AD-A063 767 MASSACHUSETTS INST OF TECH LEXINGTON LINCOLN LAB F/G 17/5
IMAGING AND TARGET DETECTION WITH A HETERODYNE-RECEPTION OPTICA--ETC(U)
OCT 78 J H SHAPIRO F19628-78-C-0002
UNCLASSIFIED TST-24 ESD-TR-78-275 NL

END
DATE FILMED
4 -79
DDC

DDC FILE COPY AD A063767

LEVEL II

12

MASSACHUSETTS INSTITUTE OF TECHNOLOGY

LINCOLN LABORATORY

IMAGING AND TARGET DETECTION WITH A HETERODYNE-RECEPTION OPTICAL RADAR

J. H. SHAPIRO
Consultant

Group 53

PROJECT REPORT TST-24
(Tactical Systems and Technology)

13 OCTOBER 1978

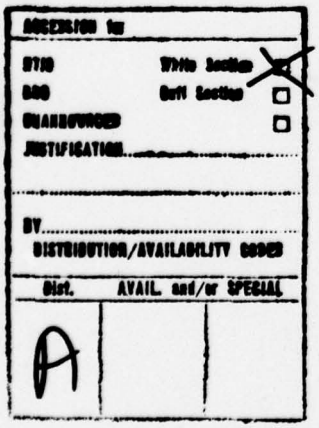

Approved for public release; distribution unlimited.

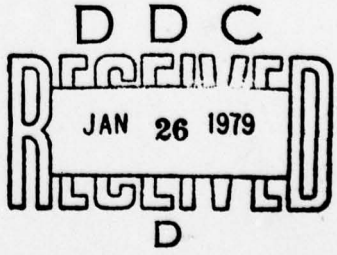

LEXINGTON

MASSACHUSETTS

ABSTRACT

A theoretical study of the use of a heterodyne reception $CO_2^{\prime\prime}$ laser radar for imaging and target detection is reported. Specifically, a mathematical system model for the radar is developed, incorporating the statistical effects of propagation through atmospheric turbulence, target speckle and glint, and heterodyne-reception shot noise. This model is used to find the image signal-to-noise ratio of a matched-filter envelope detector receiver and the target-detection probability of the optimum likelihood-ratio processor. For realistic parameter values it is shown that turbulence-induced beam spreading and coherence loss may be neglected. Target speckle and atmospheric scintillation, however, present serious limitations on single-frame imaging and target detection performance.

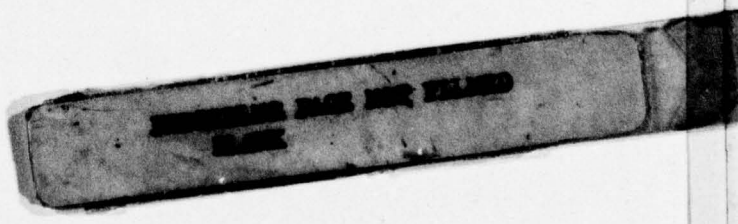

CONTENTS

	ABSTRACT	iii
I.	INTRODUCTION	1
	I.1 CO_2 Laser Radar Configuration	2
	I.2 Outline of the Report	8
II.	CLEAR-ATMOSPHERE PROPAGATION MODEL	12
	II.1 The Extended Huygens-Fresnel Principle	14
	II.2 Application to the Radar Configuration	18
III.	TARGET INTERACTION MODEL	22
	III.1 Planar Reflection Model	23
	III.2 Statistical Model for $\underline{T}(\bar{\rho}')$	26
	III.3 Relationship to Bidirectional Reflectance	28
IV.	IMAGE SIGNAL-TO-NOISE RATIO	31
	IV.1 SNR Analysis	32
	IV.2 The Single-Glint Approximation	37
	IV.3 SNR Examples	41
V.	RECEIVER OPERATING CHARACTERISTIC FOR TARGET DETECTION	53
	V.1 The Likelihood-Ratio Test	56
	V.2 The Receiver Operating Characteristic	58
VI.	SUMMARY	64
ACKNOWLEDGMENTS		73
REFERENCES		74

I. INTRODUCTION

The proliferation of optical technology that has followed the invention of the laser offers new technical options for a variety of tactical target detection and imaging scenarios. In particular, both pulsed laser range-finders and imaging radars are promising candidates for immediate development and deployment [1], [2]. The present document constitutes a theoretical study of the use of a heterodyne-reception CO_2 laser radar for target imaging and detection. This study had three primary objectives:

1) the development of a mathematical system model for the CO_2 radar, incorporating the statistical effects of the propagation medium, the target characteristics, and the heterodyne-detection process;

2) the use of this system model to investigate the influence and interplay of propagation and target effects on imaging and target detection performance;

3) the identification of areas where there are significant gaps in the knowledge needed to quantify the operational characteristics of the CO_2 radar.

It seemed clear, a priori, that the entire area of weather effects, i.e., the propagation characteristics of the atmosphere under low-visibility conditions, was poorly understood [3]-[6]. On the other hand, the propagation effects encountered in clear-weather conditions, i.e., those due to atmospheric turbulence, are now well known and adequately described by relatively convenient theoretical models [7]-[10]. Moreover,

reasonable statistical models are also available for ad hoc characterization of optical targets [11]-[13]. Thus, in addressing the preceding objectives, the system modeling and performance analysis was carried out only for clear-weather propagation conditions. As succeeding sections will testify, this choice permitted explicit derivations of the signal-to-noise ratio of an imaging radar and the receiver operating characteristic (detection probability vs. false-alarm probability) for target detection. Furthermore, the intuitive understanding gained from the clear-weather analysis has proven valuable in preliminary assessment of low-visibility system performance. The remainder of this introductory section is devoted to specifying the radar configuration that was studied, and outlining the results that were obtained.

I.1 CO_2 Laser Radar Configuration

For the purposes of statistical system-modeling, a heterodyne-reception CO_2 laser radar may be represented by the block diagram of Fig. 1. In order to make this block diagram conform with CO_2 systems under experimental investigation, the following assumptions will be made at the outset.

The transmitter and receiver will be taken to be co-located (i.e., the radar is monostatic) with common exit/entrance optics arbitrarily assumed to have an unobscured circular pupil of diameter d in the range $5 \text{ cm} \leq d \leq 20 \text{ cm}$. The transmitter laser will be assumed to produce a periodic train of rectangular-envelope purely sinusoidal pulses as shown in Fig. 2. The local oscillator will be assumed to operate in a continuous-wave (cw) mode producing an ideal monochromatic wave displaced in frequency

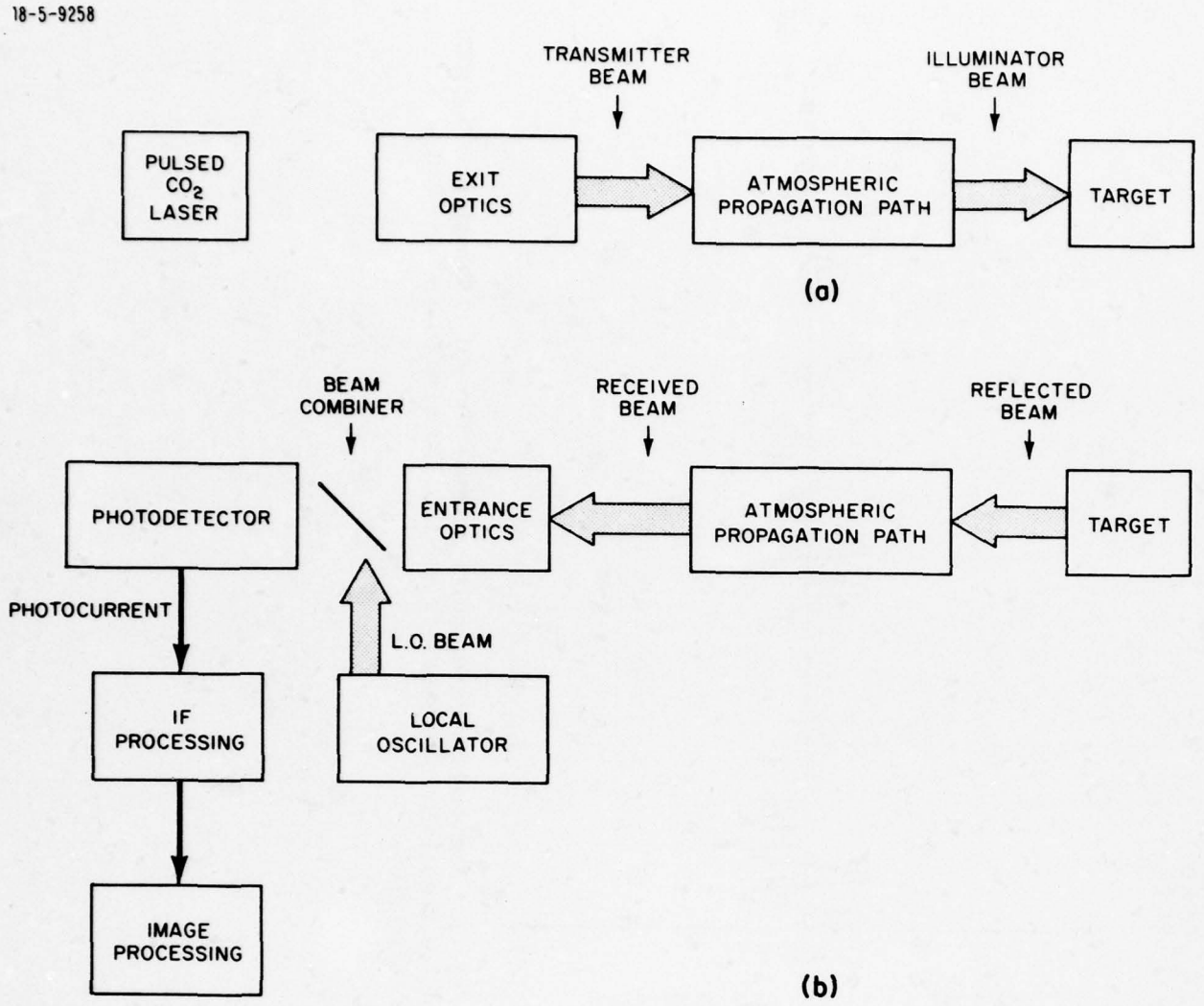

Fig. 1. CO_2 laser radar configuration: (a) transmitter-to-target path, (b) target-to-receiver path.

18-5-9259

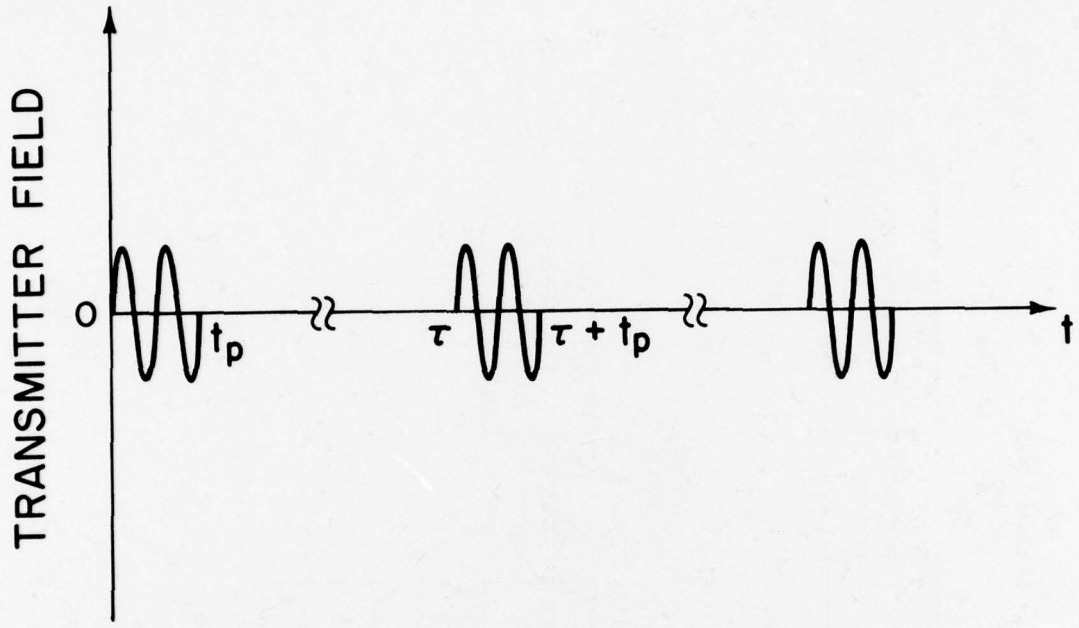

Fig. 2. Transmitter-laser pulse stream; the pulse duration is t_p-sec, pulse repetition frequency is τ^{-1} Hz, the time scale has been exaggerated.

by an amount ν_{IF} (the intermediate frequency) from the carrier frequency of the transmitter; the local oscillator power level will be assumed sufficient for shot-noise limited heterodyne reception [14].

The target of interest will be located a distance L from the radar along a line-of-sight propagation path through the clear turbulent atmosphere; L-values of interest will lie in the range 1 km $\leq$ L $\leq$ 10 km. In general, targets will be allowed to have both specular ("glint") and diffuse ("speckle") reflection components.

Mathematically, the foregoing assumptions, in concert with the transmitter pulse durations and pulse repetition frequencies and target depths forseen in realistic applications [1], [2], have the following implications. For single-pulse target detection and imaging, we may assume:

(1) The transmitted wave has a monochromatic linearly polarized electric field whose complex envelope is

$$\underline{E}_T(\bar{\rho}) = (2P_T/c\varepsilon_o)^{1/2}\, \underline{\xi}_T(\bar{\rho}), \qquad (I.1)$$

for $\bar{\rho} = (x,y)$ a two-dimensional vector in the transmitter's exit pupil. In Eq. (I.1) P_T is the pulse peak power, c is the speed of light, ε_o is the vacuum permittivity, and $\underline{\xi}_T$ is the normalized (square-integral unity over the transmitter pupil) spatial mode that is transmitted. Thus, for example,

$$\underline{\xi}_T(\bar{\rho}) = (4/\pi d^2)^{1/2}, \qquad (I.2)$$

for $|\bar{\rho}| \leq d/2$ corresponds to a collimated beam propagating in

79 01 22 048

the +z direction.

(2) The atmospheric propagation path may be assumed to be a time-independent, non-depolarizing, linear stochastic spatial system [9], [10], [15]-[18]. Thus, the complex envelope of the electric field arriving from the transmitter in the z = L plane, $\underline{E}_t(\bar{\rho}')$ for $\bar{\rho}' = (x',y')$, satisfies

$$\underline{E}_t(\bar{\rho}') = \int d\bar{\rho}\ \underline{E}_T(\bar{\rho})\ \underline{h}_L(\bar{\rho}',\bar{\rho}). \tag{I.3}$$

In Eq. (I.3), $\underline{h}_L$ is the stochastic atmospheric Green's function.

(3) The target interaction may be assumed to occur on the plane z = L so that the complex envelope of the electric field in the z = L plane that is directed back towards the transmitter satisfies

$$\underline{E}_r(\bar{\rho}') = \underline{E}_t(\bar{\rho}')\ \underline{T}(\bar{\rho}') \tag{I.4}$$

where $\underline{T}(\bar{\rho}')$ is the complex-field reflection coefficient of the target at the point $\bar{\rho}'$. This reflection coefficient will in general be stochastic as it includes both glint and speckle components.

(4) Because of atmospheric reciprocity [15], the complex envelope of the electric field in the receiver entrance pupil, $\underline{E}_R(\bar{\rho})$, satisfies

$$\underline{E}_R(\bar{\rho}) = \int d\bar{\rho}'\ \underline{E}_r(\bar{\rho}')\ \underline{h}_L(\bar{\rho}',\bar{\rho}). \tag{I.5}$$

Note that the same Green's function appears in both Eqs. (I.3) and (I.5).

(5) Because of the antenna theorem for heterodyne reception [19], the local-oscillator field and the photodetection process may be described as though they were present in the receiver's entrance pupil. Thus, assuming a local oscillator complex envelope $\underline{E}_\ell(\bar{\rho})$ given by

$$\underline{E}_\ell(\bar{\rho}) = (2P_\ell/c\varepsilon_o)^{1/2}\, \underline{\xi}_\ell(\bar{\rho})\, \exp(j2\pi\nu_{IF}t) \qquad (I.6)$$

where P_ℓ is the local-oscillator power, and $\underline{\xi}_\ell(\bar{\rho})$ is a normalized spatial mode, the passband-filtered amplified photocurrent (IF signal) takes the form

$$r(t) = \mathrm{Re}\,[\underline{r}(t)\exp\,(-j2\pi\nu_{IF}t)] \qquad (I.7)$$

where the complex envelope $\underline{r}(t)$ satisfies [14]

$$\underline{r}(t) = (c\varepsilon_o/2)^{1/2}\int d\bar{\rho}\; \underline{E}_R(\bar{\rho})\underline{\xi}_\ell^*(\bar{\rho})+\underline{n}(t). \qquad (I.8)$$

In Eq. (I.8), $\underline{n}(t)$ is a zero-mean circulo-complex Gaussian noise process whose power spectral density is (assuming a rectangular passband filter at the IF frequency)

$$S_{nn}(f) = h\nu_o/\eta, \text{ for } |f| \leq W \qquad (I.9)$$

where ν_o is the transmitter optical frequency, η is the quantum efficiency of the photodetector, and 2W is the unilateral IF bandwidth. Because the transmitter is actually pulsed, Eq. (I.8)

assumes $W \geq 1/t_p$. Note that for maximum heterodyne-detection efficiency $\underline{\xi}_\ell(\bar{\rho}) = \underline{E}_R(\bar{\rho})/\left(\int d\bar{\rho}|\underline{E}_R(\bar{\rho})|^2\right)^{1/2}$ is required. In practice, however, $\underline{\xi}_\ell(\bar{\rho}) = \underline{\xi}_T^*(\bar{\rho})$ is generally employed, and often approximates the previous condition.

The preceding mathematical characterization of the laser radar is summarized in Fig. 3 and Table 1. How the IF signal, r(t), is processed depends on whether the system is to be used for imaging or target detection. In the former instance, r(t) is to be used to estimate the average target reflection strength; ordinarily this will involve matched-filter envelope detection, i.e., determining $|t_p^{-1}\int_0^{t_p}\underline{r}(t)dt|^2$, followed by computer enhancement. (Note that a single photodetector has been assumed so that a target image must be built up by scanning the transmitter beam using a series of pulses. The extension of the model of Eqs. (I.8), (I.9) to the case of array detection can be accomplished, but will be omitted.) In the target-detection application, r(t) is to be used to determine the presence or absence of a reflector in the z = L plane; ordinarily this would be accomplished by comparing $|t_p^{-1}\int_0^{t_p}\underline{r}(t)dt|^2$ with a threshold value.

I.2 Outline of the Report

The remainder of this report is organized as follows. In Section II there is a tutorial presentation of the extended Huygens-Fresnel principle description of optical wave propagation through atmospheric turbulence. Thus material, which comprises a statistical characterization of the Green's function $\underline{h}_L$ appearing in Eqs. (I.3), (I.5), will be couched in terms which emphasize the physical effects of turbulence on the fields

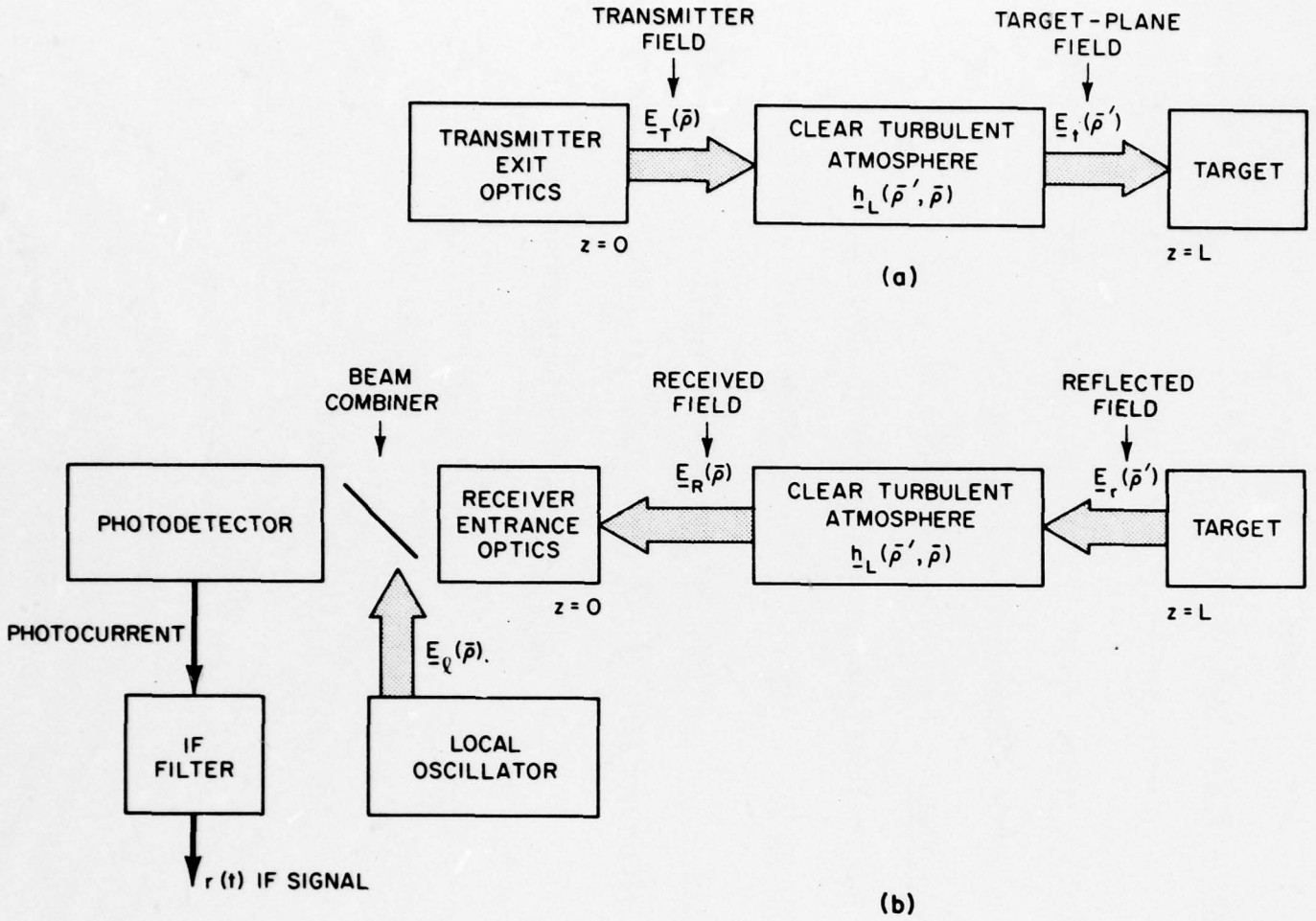

Fig. 3. Summary of CO_2 laser radar model: (a) transmitter-to-target path, (b) target-to-receiver path.

TABLE I

SUMMARY OF CO_2 LASER RADAR MODEL

TRANSMITTER FIELD $\underline{E}_T(\bar{\rho}) = (2\,P_T/\,c\varepsilon_o)^{1/2}\,\underline{\xi}_T(\bar{\rho})$ in z = 0 plane

P_T = transmitter power, $\underline{\xi}_T(\bar{\rho})$ = normalized spatial mode of transmitter

TARGET-PLANE FIELD $\underline{E}_t(\bar{\rho}') = \int d\bar{\rho}\;\underline{E}_T(\bar{\rho})\;\underline{h}_L(\bar{\rho}',\,\bar{\rho})$ in z = L plane

$\underline{h}_L(\bar{\rho}',\,\bar{\rho})$ = atmospheric Green's function

REFLECTED FIELD $\underline{E}_r(\bar{\rho}') = \underline{E}_t(\bar{\rho}')\;\underline{T}(\bar{\rho}')$ in z = L plane

$\underline{T}(\bar{\rho}')$ = target complex-field reflection coefficient

RECEIVED FIELD $\underline{E}_R(\bar{\rho}) = \int d\bar{\rho}'\;\underline{E}_r(\bar{\rho}')\;\underline{h}_L(\bar{\rho}',\bar{\rho})$ in z = 0 plane

IF SIGNAL $r(t) = \mathrm{Re}[\underline{r}(t)\exp(-j2\pi\nu_{IF}t)]$

$\underline{r}(t) = (c\varepsilon_o/2)^{1/2}\int d\bar{\rho}\;\underline{E}_R(\bar{\rho})\;\underline{\xi}_\ell^*(\bar{\rho}) + \underline{n}(t)$, $\underline{n}(t)$ = receiver noise,

$\underline{\xi}_\ell(\bar{\rho})$ = local-oscillator spatial mode

$\underline{E}_t(\bar{\rho}')$ and $\underline{E}_R(\bar{\rho})$. (These are the fields which illuminate the target and the receiver's entrance pupil, respectively.) It will be shown that for the values of d, L of interest the primary effect of turbulence on the CO_2 laser radar will be due to scintillation, i.e., beam spreading on $\underline{E}_t(\bar{\rho}')$ will usually be negligible as will be spatial coherence loss on $\underline{E}_R(\bar{\rho})$.

In Section III, a statistical model for the target reflection coefficient $\underline{T}(\bar{\rho}')$ will be discussed. The physical origins of the glint and speckle components will be described, as well as their determination from bidirectional reflectance data. This determination is particularly important, in view of the wealth of bidirectional reflectance data that has been accumulated for various target materials and shapes [20].

In Section IV, these results are brought together to derive the signal-to-noise ratio (SNR) obtained from matched-filter envelope detection. A number of numerical examples are presented to illustrate the various contributions of glint, speckle, scintillation, and shot noise to image SNR. These examples will indicate the importance of multi-frame averaging to obtaining satisfactory image quality.

In Section V, the optimum detection of target presence or absence is analyzed. Results will be presented for the receiver operating characteristic (ROC) in the presence of a pure glint or pure speckle target. The need for further numerical work will be indicated.

The material that will be presented in Sections II-V is a substantially complete analysis of clear-weather laser radar operation. A summary of the key results of this work will be given in Section VI.

II. CLEAR-ATMOSPHERE PROPAGATION MODEL

Under clear-weather conditions at an operating wavelength for which molecular absorption is insignificant, the atmosphere as an optical propagation medium differs from free space in that the former exhibits random spatio-temporal refractive index fluctuations. We shall refer to these refractive index fluctuations, which are due to turbulent mixing of air parcels with approximately 1°K temperature differences, as atmospheric turbulence. Although the refractive index variations encountered in turbulent air are only a few parts in 10^6, their effect on optical wave propagation is profound.

At a qualitative level, we may gain an appreciation for turbulence-induced propagation effects as follows. Let us regard an instantaneous array of atmospheric refractive-index eddies as an array of randomly shaped blobs with nominal spatial scales ranging from an inner scale $\ell_o \approx 10^{-3}$ m to an outer scale $L_o \approx 10 - 10^2$ m, as shown in Fig. 4, and various refractive-index values. Consider the effects of placing an h meter layer of such turbulence in the propagation path between the radar and the target in the geometry of Fig. 3 with $h << L$. Phenomenologically, we have the following situation:

Transmitter beam spread If the turbulent layer is near the radar it will randomly dephase the transmitted field $\underline{E}_T(\bar{\rho})$. In particular, when the transmitter exit pupil diameter, d, exceeds the transverse phase-coherence scale of the turbulence, the effective transmitter beamwidth will be turbulence limited rather than diffraction limited. When the turbulent

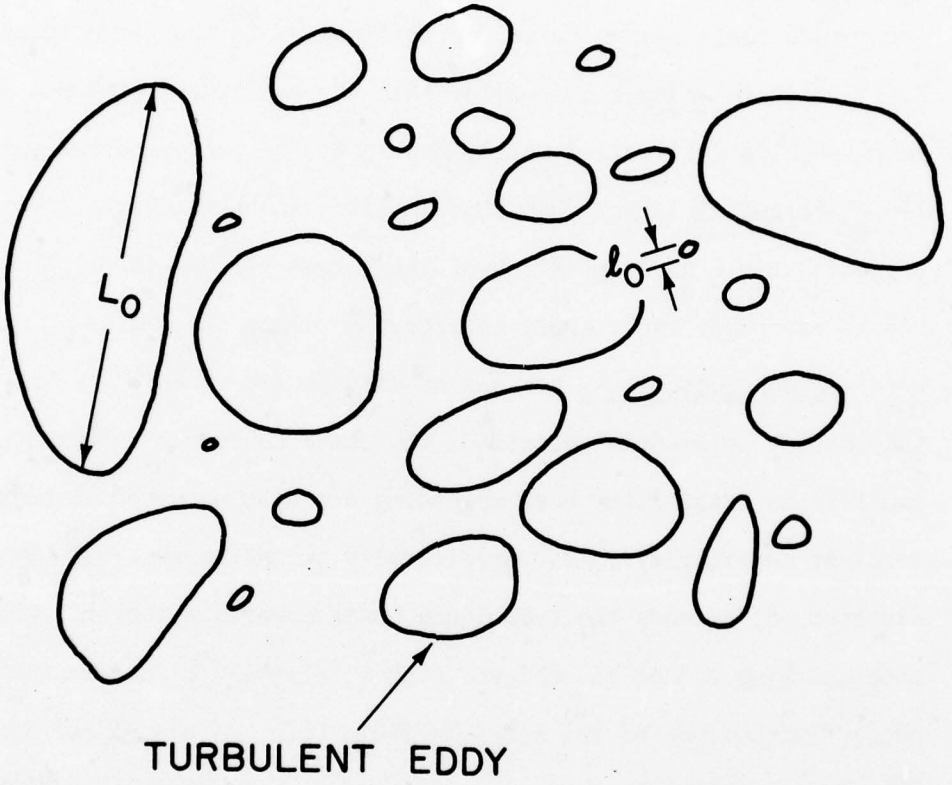

Fig. 4. Schematic representation of an array of turbulent eddies with different refractive index values; ℓ_o is the inner scale, L_o is the outer scale of the Kolmogorov inertial subrange.

layer is located close to the target, there will be essentially no transmitter beam spreading.

Target-plane scintillation The random lensing of the transmitter beam by the turbulent layer leads to constructive and destructive interference (amplitude fluctuations called scintillation) in the target-plane field $\underline{E}_t(\bar{\rho}')$. If the target is smaller than the amplitude-coherence scale of the turbulence, scintillation merely modulates the reflected radiant intensity. If the target is larger than this amplitude-coherence scale, scintillation presents itself as a speckling of the target illumination, $|\underline{E}_t(\bar{\rho}')|^2$, which the receiver may incorrectly interpret as image information.

Receiver coherence loss Because of atmospheric reciprocity and the antenna theorem for heterodyne reception, the phase coherence effects that were manifest as transmitter beam spreading are also observed as heterodyne-receiver sensitivity loss. Specifically, when the receiver entrance pupil diameter, d, exceeds the turbulence phase-coherence length, optimum spatial-mode matching cannot be achieved with $\underline{\xi}_\ell(\bar{\rho}) = \underline{\xi}^*_T(\bar{\rho})$ due to the random phase fluctuations of the received field $\underline{E}_R(\bar{\rho})$. This effect is pronounced when the turbulent layer is near the radar, and essentially absent when the turbulent layer is near the target.

II.1 The Extended Huygens-Fresnel Principle

During the past decade, the propagation physics community has taken enormous strides towards achieving a comprehensive theory for wave propagation in the turbulent atmosphere [7]-[10], [21]. In this section, we shall summarize the extended Huygens-Fresnel principle (the linear-system)

model for atmospheric propagation [9], [10], [15], [17], [18], [22]-[25], wherein the statistics of a field received from an arbitrary extended source are obtained, through a superposition integral, from the statistics of a spherical wave (point source). This approach to the propagation problem will quantify the qualitative effects we have just described in a form amenable to image SNR and target detection ROC calculations.

In the absence of turbulence, free-space scalar paraxial propagation theory [26] tells us that

$$\underline{E}_t(\bar{\rho}') = \int d\bar{\rho}\ \ \underline{E}_T(\bar{\rho})\ (j\lambda L)^{-1} \exp[jkL(1 + |\bar{\rho}'-\bar{\rho}|^2/2L^2)], \qquad \text{(II.1)}$$

and

$$\underline{E}_R(\bar{\rho}) = \int d\bar{\rho}'\ \ \underline{E}_r(\bar{\rho}')\ (j\lambda L)^{-1} \exp[jkL(1 + |\bar{\rho}'-\bar{\rho}|^2/2L^2)], \qquad \text{(II.2)}$$

where $\lambda = c/\nu_o$, $k = 2\pi/\lambda$ are the wavelength and wavenumber at the transmitter frequency ν_o. Equations (II.1), (II,2) comprise the Huygens-Fresnel principle and the reciprocity theorem of Helmholtz; note that they are of the forms assumed in (I.3), (I.5). In the presence of turbulence, the extended Huygens-Fresnel principle and atmospheric reciprocity tell us that (I.3), (I.5) are valid with

$$\underline{h}_L(\bar{\rho}', \bar{\rho}) = (j\lambda L)^{-1} \exp[jkL(1 + |\bar{\rho}'-\bar{\rho}|^2/2L^2)]$$

$$\text{x } \exp\ (\chi(\bar{\rho}', \bar{\rho}) + j\phi(\bar{\rho}', \bar{\rho})), \qquad \text{(II.3)}$$

where χ and ϕ are real valued turbulence induced log-amplitude and phase perturbations respectively. Physically, $\chi(\bar{\rho}', \bar{\rho})$ $(\phi(\bar{\rho}', \bar{\rho}))$ is the log-

amplitude (phase) perturbation of the field measured at the point $\bar{\rho}'$ in the z=L plane from a point source located at the point $\bar{\rho}$ in the z=0 plane. (Via reciprocity, the roles of transmitter and receiver may be interchanged in the foregoing interpretation.) Mathematically, it is usually valid to assume that χ and ϕ are jointly Gaussian stochastic processes with known means and covariances. For the calculations to be made in the sequel, we shall need only the following results:

Wave-structure function The two-source spherical-wave wave structure function defined by

$$D(\bar{\rho}', \bar{\rho}) = \langle[\chi(\bar{\rho}_1' + \bar{\rho}', \bar{\rho}_1 + \bar{\rho}) - \chi(\bar{\rho}_1', \bar{\rho}_1)]^2\rangle + \langle[\phi(\bar{\rho}_1' + \bar{\rho}', \bar{\rho}_1 + \bar{\rho}) - \phi(\bar{\rho}_1', \bar{\rho}_1)]^2\rangle, \quad \text{(II.4)}$$

where angular brackets denote ensemble average, satisfies

$$D(\bar{\rho}', \bar{\rho}) = 2.91\, k^2 \int_0^L dz C_n^2(z)\, (|\bar{\rho}'z + \bar{\rho}(L-z)|/L)^{5/3} \quad \text{(II.5)}$$

for Kolmogorov-spectrum turbulence with $C_n^2(z)$ being the turbulence strength profile along the path from the radar (z = 0) to the target (z = L). In terms of this wave structure function we have that the Green's function mutual coherence function is

$$\langle \underline{h}_L(\bar{\rho}_1' + \bar{\rho}', \bar{\rho}_1 + \bar{\rho})\, \underline{h}_L^*(\bar{\rho}_1', \bar{\rho}_1)\rangle = (\lambda L)^{-2} \exp[jk(|\bar{\rho}_1' - \bar{\rho}_1 + \bar{\rho}' - \bar{\rho}|^2 - |\bar{\rho}_1' - \bar{\rho}_1|^2)/2L] \times \exp(-D(\bar{\rho}', \bar{\rho})/2). \quad \text{(II.6)}$$

Log-amplitude covariance function The two-source log-amplitude covariance function, defined by

$$C_{\chi\chi}(\bar{\rho}', \bar{\rho}) = \langle[\chi(\bar{\rho}_1' + \bar{\rho}', \bar{\rho}_1 + \bar{\rho}) - m_\chi][\chi(\bar{\rho}_1', \bar{\rho}_1) - m_\chi]\rangle, \quad \text{(II.7)}$$

where m_χ is the (assumed) space-independent mean value of $\chi(\bar{\rho}', \bar{\rho})$, is given in the weak perturbation regime by

$$C_{\chi\chi}(\bar{\rho}', \bar{\rho}) =$$

$$4\pi^2k^2\int_0^L dz \int_0^\infty du\, u\, C_n^2(z)S_n(u)J_o(du)\sin^2[u^2z(L-z)/2kL] \quad \text{(II.8)}$$

in terms of an arbitrary refractive index spectrum $S_n(u)$ with $d = |\bar{\rho}'\, z + \bar{\rho}(L - z)|/L$. Equation (II.8) has been evaluated when $\bar{\rho} = \bar{0}$ for Kolmogorov-spectrum turbulence and a uniform C_n^2 profile; the resulting correlation length for the log amplitude is approximately the Fresnel-zone length $(\lambda L)^{1/2}$. The preceding weak-perturbation results are valid when $\sigma^2_\chi \equiv C_{\chi\chi}(\bar{0}, \bar{0}) \leq 0.5$; appreciably larger values of the log-amplitude variance are not encountered (a phenomenon known as saturation of scintillation). It is almost always reasonable to assume $m_\chi = -\sigma^2_\chi$, a condition which amounts to conservation of average irradiance. For Kolmogorov spectrum turbulence with a uniform C_n^2 profile

$$\sigma^2_\chi = 0.124\, C_n^2\, k^{7/6}\, L^{11/6}. \quad \text{(II.9)}$$

II.2 Application to the Radar Configuration

Let us apply the model of Section II.1 to the radar configuration of Fig. 3. Specifically, let us quantify the propagation phenomena that we have described qualitatively:

Transmitter beam spread The average target-plane irradiance that results from transmission of $\underline{E}_T(\bar{\rho})$ through L meters of turbulent air with turbulence strength profile $C_n^2(z)$, $0 \leq z \leq L$ satisfies

$$\langle|\underline{E}_t(\bar{\rho}')|^2\rangle = \langle\left|\int d\bar{\rho}\ \underline{E}_T(\bar{\rho})\ \underline{h}_L(\bar{\rho}', \bar{\rho})\right|^2\rangle \qquad \text{(II.10)}$$

from (I.3). From (II.3)-(II.6) we obtain

$$\langle|\underline{E}_t(\bar{\rho}')|^2\rangle = \int d\bar{\rho}_1 \int d\bar{\rho}_2\ \underline{E}_T(\bar{\rho}_1)\ \underline{E}_T^*(\bar{\rho}_2)(\lambda L)^{-2}$$

$$\times \exp[jk(|\bar{\rho}_1|^2 - |\bar{\rho}_2|^2)/2L - jk\bar{\rho}' \cdot (\bar{\rho}_1 - \bar{\rho}_2)/L - D(\bar{0}, \bar{\rho}_1 - \bar{\rho}_2)/2] \qquad \text{(II.11)}$$

where $D(\bar{0}, \bar{\rho}) = (|\bar{\rho}|/\rho_o)^{5/3}$ for $\rho_o \equiv [2.91\ k^2 \int_0^L dz\ C_n^2(z)(1-z/L)^{5/3}]^{-3/5}$. The quantity ρ_o is the turbulence field (or phase) coherence length in the transmitter exit pupil plane. Thus, when $d \ll \rho_o$ we expect (and, indeed, from (II.11) we find) that $\langle|\underline{E}_t(\bar{\rho}')|^2\rangle$ is given by the free-space target-plane irradiance pattern. Furthermore, when $d > \rho_o$ and $\underline{E}_T(\bar{\rho})$ is, for example, a collimated-beam mode, $\langle|\underline{E}_t(\bar{\rho}')|^2\rangle$ will exhibit severe turbulence-induced beam spreading. Note that, in accord with our intuitive discussion, ρ_o weights turbulence located near the radar transmitter much more heavily than it does turbulence located near the target. It remains only for us to

evaluate ρ_o in order to assess the likelihood of turbulence-induced transmitter beam spreading. In Fig. 5 we have plotted ρ_o vs. L for several values of C_n^2 assuming 10.6μ radiation and a uniform turbulence strength profile along the path. Because C_n^2 falls off inversely with altitude in a fairly rapid manner (below the tropopause), it would appear that the CO_2 radar with 5 cm $\leq$ d $\leq$ 20 cm will only suffer from transmitter beam spreading, over the path lengths of interest, under conditions of strong turbulence.

Target-plane scintillation We shall assume henceforth that $d < \rho_o$ so that for $|\bar{\rho}| \leq d/2$ we may employ $\chi(\bar{\rho}', \bar{\rho}) \tilde{\approx} \chi(\bar{\rho}', \bar{0})$, $\phi(\bar{\rho}', \bar{\rho}) \tilde{\approx} \phi(\bar{\rho}', \bar{0})$. We thus find that the target-plane field (prior to reflection) is

$$\underline{E}_t(\bar{\rho}') \tilde{\approx} (2P_T/c\varepsilon_o)^{1/2} \underline{\xi}_t(\bar{\rho}') \exp(\chi(\bar{\rho}', \bar{0}) + j\phi(\bar{\rho}', \bar{0})), \qquad \text{(II.12)}$$

where

$$\underline{\xi}_t(\bar{\rho}') \equiv \int d\bar{\rho}\, \underline{\xi}_T(\bar{\rho})(j\lambda L)^{-1} \exp[jkL(1 + |\bar{\rho}' - \bar{\rho}|^2/2L^2)] \qquad \text{(II.13)}$$

is the normalized free-space target plane field mode generated by transmission of $\underline{\xi}_T(\bar{\rho})$. Equation (II.12) shows the target-plane scintillation effect through the presence of the $\chi(\bar{\rho}', \bar{0})$ term. For a uniform turbulence-strength profile, 10.6μ wavelength radiation will not encounter saturation of scintillation at path lengths of interest except under conditions of strong turbulence (see Fig. 6). Thus, we may generally employ the weak-perturbation regime $(\lambda L)^{1/2}$ coherence length for $\chi(\bar{\rho}', \bar{0})$.

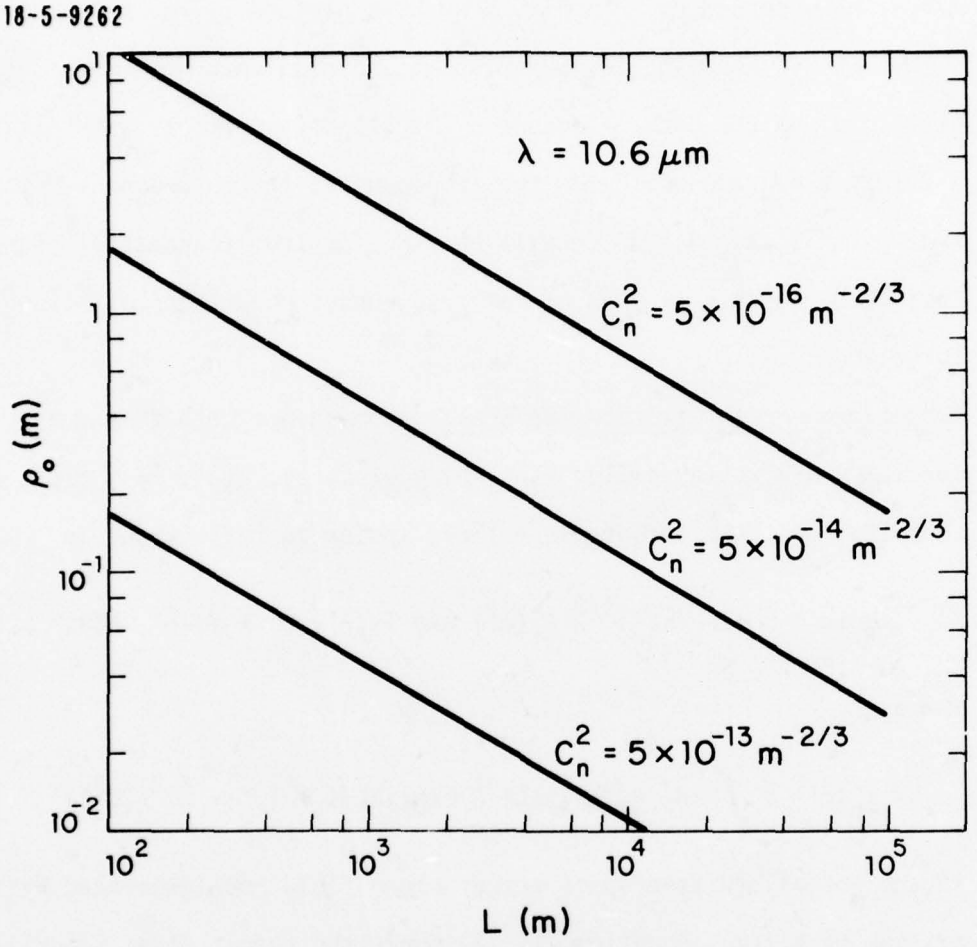

Fig. 5. Turbulence field coherence length ρ_o vs propagation path length L for conditions of weak turbulence ($C_n^2 = 5 \times 10^{-16}\ m^{-2/3}$) moderate turbulence ($C_n^2 = 10^{-14}\ m^{-2/3}$) and strong ($C_n^2 = 5 \times 10^{-13}\ m^{-2/3}$) turbulence; 10.6 μm wavelength has been assumed throughout.

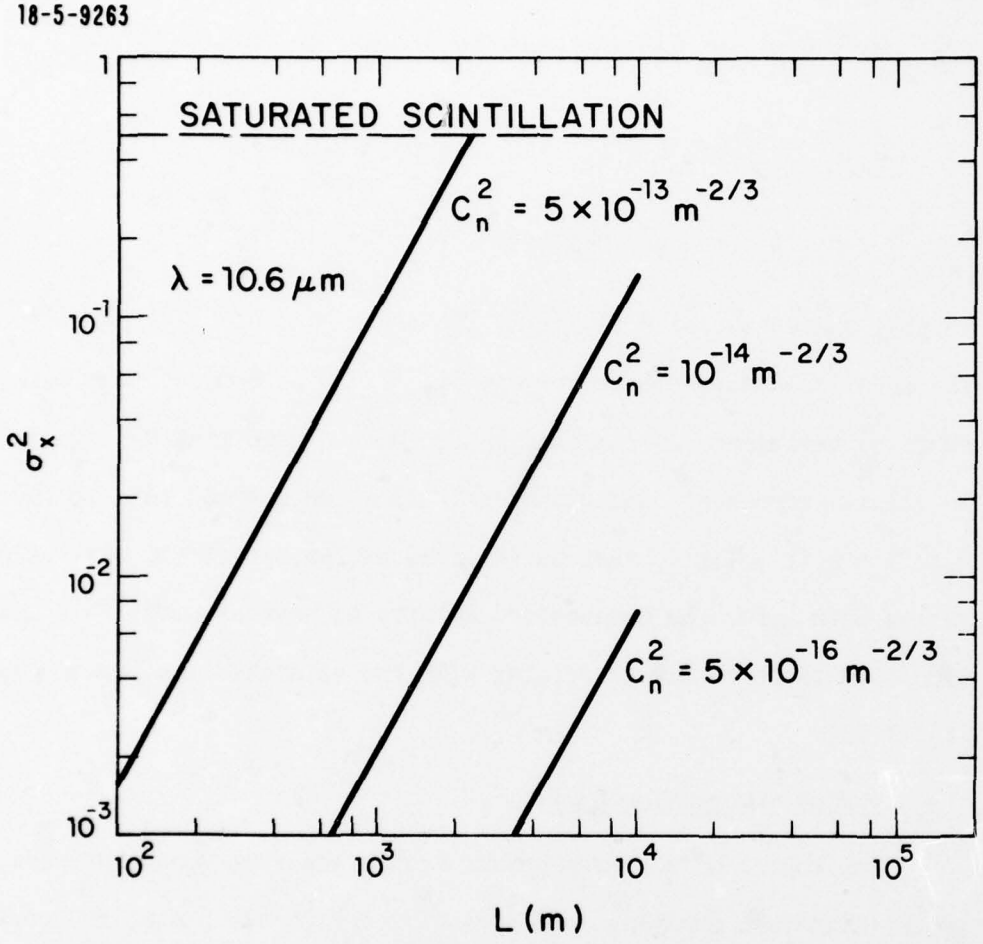

Fig. 6. Log-amplitude various σ_χ^2 vs propagation path length L for weak ($C_n^2 = 5 \times 10^{-16}\ m^{-2/3}$), moderate ($C_n^2 = 10^{-14}\ m^{-2/3}$), and strong ($C_n^2 = 5 \times 10^{-13} m^{-2/3}$) turbulence; 10.6 μm wavelength is assumed and the weak perturbation theory is employed.

Receiver coherence loss Assuming $d << \rho_o$, there will be negligible receiver coherence loss to affect the heterodyne reception of $\underline{E}_R(\bar{\rho})$. We have, using $\chi(\bar{\rho}', \bar{\rho}) \approx \chi(\bar{\rho}', \bar{0})$ and $\phi(\bar{\rho}', \bar{\rho}) \approx \phi(\bar{\rho}', \bar{0})$ for $|\bar{\rho}| \leq d/2$, that

$$\underline{E}_R(\bar{\rho}) \approx \int d\bar{\rho}\, \underline{E}_r(\bar{\rho}')\, (j\lambda L)^{-1} \exp\,[jkL(1 + |\bar{\rho}' - \bar{\rho}|^2/2L^2)]$$

$$\times \exp\,(\chi(\bar{\rho}', \bar{0}) + j\phi(\bar{\rho}', \bar{0})) \qquad \text{(II.14)}$$

so that the essential behavior of the phasefront of $\underline{E}_R(\bar{\rho})$ is given by the spherical curvature factor $\exp(jk|\bar{\rho}|^2/2L)$ as would be the case were there no turbulence in the propagation path. Note that the $\chi(\bar{\rho}', \bar{0})$ term in (II.14) represents additional scintillation, beyond that included in $\underline{E}_r(\bar{\rho}') = \underline{E}_t(\bar{\rho}')\, \underline{T}(\bar{\rho}')$, that is incurred on the target-to-receiver propagation path. For the monostatic geometry we have assumed, this scintillation term is perfectly correlated with the scintillation term encountered in (II.12).

III. TARGET INTERACTION MODEL

The topics of electromagnetic scattering from rough surfaces, radar target-signature analysis, and optical speckle have a vast and growing literature (see, for example, [12], [20], [27]-[31]). Our purpose in the present section is to propose a statistical model for target interaction that is analytically tractable yet incorporates the accepted target phenomenology of glint plus speckle reflections. We shall begin with a brief description of these reflection characteristics.

III.1 Planar Reflection Model

In scalar paraxial optics, when an optical beam which propagates nominally along the +z axis encounters a polished spherical surface of intensity reflection coefficient Γ whose center of curvature lies on or near the z-axis and whose radius of curvature greatly exceeds the beam diameter of the impinging wave a planar reflection model may be used. As shown in Fig. 7, if we designate a constant-z plane that is near the reflecting surface as the input/output plane, this means we can assume that the reflected field $\underline{E}_r(\bar{\rho}')$ is given in terms of the incident field $\underline{E}_t(\bar{\rho}')$ by the expression

$$\underline{E}_r(\bar{\rho}') = \underline{E}_t(\bar{\rho}')\ \Gamma^{1/2}\ \exp(-jk|\bar{\rho}' - \bar{\rho}'_c|^2/R_c) \qquad \text{(III.1)}$$

for $|\bar{\rho}'| \leq$ target radius where R_c is the radius of curvature, $\bar{\rho}'_c$ is the transverse location of the center of curvature for the surface, and we have suppressed a $\bar{\rho}'$ - independent phase factor.

For a more general polished reflecting surface, with smoothly varying intensity reflection coefficient, local radius and center of curvature, the paraxial theory leads to an input/output relation of the form[1]

$$\underline{E}_r(\bar{\rho}') = \underline{E}_t(\bar{\rho}')\ \Gamma^{1/2}(\bar{\rho}')\ \exp(-jk|\bar{\rho}' - \bar{\rho}'_c(\bar{\rho}')|^2/R_c(\bar{\rho}')) \qquad \text{(III.2)}$$

---

[1] It would be somewhat more general to allow for locally-ellipsoidal surfaces. We shall not do so as (III.2) is sufficient for the physical arguments needed here and in the single-glint approximation.

18-5-9264

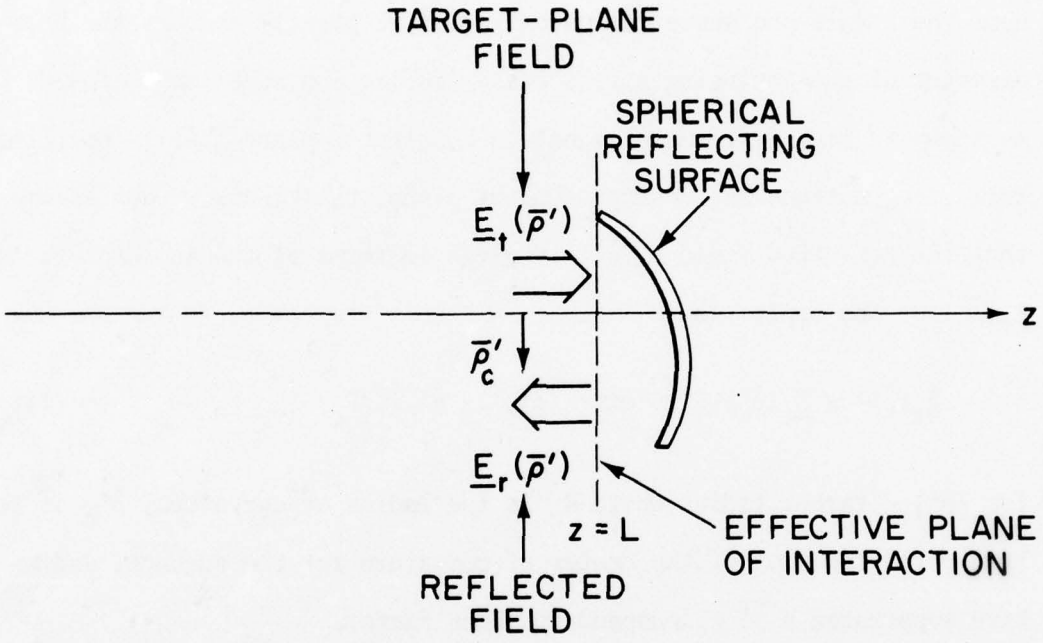

Fig. 7. Geometry of the planar-reflection model for a polished spherical reflector; the reflected field satisfies Eq.(III.1) where, for the surface shown, $R_c > 0$.

We shall assume that for all targets of interest we can assign a constant-z plane to be an input/output plane for the target interaction in the sense that the incident and reflected fields are related by

$$\underline{E}_r(\bar{\rho}') = \underline{E}_t(\bar{\rho}')\ \underline{T}(\bar{\rho}'). \tag{III.3}$$

Equation (III.3) is the model mentioned in Section I.1. For polished surfaces with smoothly varying characteristics, $\underline{T}$, the target field reflection coefficient, is given explicitly in (III.2). For such targets $\underline{T}(\bar{\rho}')$ characterizes both the reflection strength and surface shape of the object through its amplitude and phase behavior. This is not the case for rough targets, or for targets which violate the paraxiality assumption (e.g., in situations in which shadowing can occur). Nevertheless in all circumstances we shall regard $\underline{T}(\bar{\rho}')$ as the target, i.e., the more the radar can determine about $\underline{T}(\bar{\rho}')$ the more it has learned about the target.

The planar reflection model Eq. (III.3) has two limiting cases. The first is the case of specular reflection. This is the limit wherein $\underline{T}$ reduces to the form of (III.2) or even (III.1). In such circumstances, the reflected field will have directionality properties comparable to those of the incident field; i.e., the target acts like a mirror (magnifying/demagnifying or distorting depending on whether (III.1) or (III.2) holds). Under favorable alignment conditions a specular object will direct a very strong reflection towards the radar receiver.

The second limit of (III.3) is that of diffuse reflection, such as will occur for objects whose surfaces are very rough on spatial scales

comparable to the wavelength of the incident field. In such circumstances, the reflected field is in essence spatially incoherent. For laser beam illumination, however, the reflected field will have temporal coherence, so that constructive and destructive interference effects will be observable in the irradiance pattern at the radar receiver. This is the well known speckle effect.

It turns out, of course, that real targets share aspects of both these limiting cases. A real target may have several "glint" components, i.e., give rise to several near-specular reflections, in addition to a virtually non-directional speckle component.

III.2 Statistical Model for $\underline{T}(\bar{\rho}')$

We propose the following statistical model for the target complex-field reflection coefficient $\underline{T}(\bar{\rho}')$ at a fixed wavelength λ. We shall arbitrarily distinguish between glint and speckle reflections by writing

$$\underline{T}(\bar{\rho}') = \underline{T}_g(\bar{\rho}')\, e^{j\theta} + \underline{T}_s(\bar{\rho}'). \tag{III.4}$$

In Eq. (III.4), $\underline{T}_g(\bar{\rho}')$ denotes the glint reflection coefficient, and $\underline{T}_s(\bar{\rho}')$ denotes the speckle reflection coefficient; these components of $\underline{T}(\bar{\rho}')$ will be characterized as follows.

Following standard practice [11]-[13], we shall ascribe $\underline{T}_s(\bar{\rho}')$ to the microscopic surface-height fluctuations (surface roughness) of the target and treat it as a statistical quantity with moments

$$\langle \underline{T}_s(\bar{\rho}') \rangle = 0, \tag{III.5}$$

$$\langle \underline{T}_s(\bar{\rho}_1') \, \underline{T}_s(\bar{\rho}_2') \rangle = 0, \tag{III.6}$$

and

$$\langle \underline{T}_s(\bar{\rho}_1') \, \underline{T}_s^*(\bar{\rho}_2') \rangle = \lambda^2 T_s(\bar{\rho}') \, \delta(\bar{\rho}_1' - \bar{\rho}_2'). \tag{III.7}$$

Equations (III.5)-(III.7) quantify the statement that a purely diffuse-reflecting target turns a spatially-coherent illumination beam into a spatially-incoherent reflected beam; the δ-function in (III.7) implies this reflected beam has essentially no directionality to it. In imaging a diffuse target, the non-random quantity $T_s(\bar{\rho}')$, which is physically the mean-square speckle-reflection coefficient at location $\bar{\rho}'$, is the target information that is sought. It turns out, however, that to calculate the image SNR for the diffuse target we must also characterize the fourth moment of $\underline{T}_s(\bar{\rho}')$. This is generally done by assuming said moment can be factored in the manner that applies when $\underline{T}_s$ is a circulo-complex Gaussian process [32]. Because we shall need a complete statistical characterization of $\underline{T}_s$ in order to evaluate the ROC for diffuse-target detection, we shall assume that $\underline{T}_s$ is a circulo-complex Gaussian process with moments (III.5)-(III.7).

The glint reflection coefficient, $\underline{T}_g(\bar{\rho}')$, models the specular reflection component that is due to the nominal (smoothly-varying) target shape. For polished targets with smoothly-varying characteristics, $\underline{T}_g(\bar{\rho}')$ will be given by (III.2). For a "semi-rough" target which has a significant speckle reflection coefficient, but still has some glint

component, we may continue to assume that $\underline{T}_g(\bar{\rho}')$ is of the form (III.2) by interpreting $\Gamma(\bar{\rho}')$ to be the local glint intensity reflection coefficient at location $\bar{\rho}'$ [13]. Such semi-rough targets will have $|\underline{T}_g(\bar{\rho}')|^2 << T_s(\bar{\rho}')$, although, because of directionality effects, the glint return may dominate the speckle return at the radar receiver entrance pupil (see Section IV). Note that $\underline{T}_g(\bar{\rho}')$ will always be treated as a deterministic quantity. The phase angle θ that appears in (III.4) will be taken to be a uniformly distributed random variable on $[0, 2\pi]$ that is statistically independent of the speckle reflection coefficient; this phase angle models our uncertainty in the location of the target plane on the scale of the radar wavelength. Although, for a purely specular target, we know that both the amplitude and phase of $\underline{T}_g(\bar{\rho}')$ contain target information, we shall assume the imaging radar is primarily interested in $|\underline{T}_g(\bar{\rho}')|^2$. For semi-rough targets, i.e., targets with non-negligible glint and speckle reflection components, the radar will be assumed to seek $<|\underline{T}(\bar{\rho}')|^2>$.

III.3 Relationship to Bidirectional Reflectance

Let us examine the relationship between the preceding target statistical model and bidirectional reflectance, the target-signature quantity that is generally measured [2], [20]. For the target geometry of Fig. 8, the bidirectional reflectance may be defined as

$$\rho'(\lambda; \bar{f}_i; \bar{f}_r) = (\lambda^2 A_T)^{-1} < \left| \int d\bar{\rho}' \exp[j2\pi(\bar{f}_i - \bar{f}_r)\cdot\bar{\rho}'] \, \underline{T}(\bar{\rho}') \right|^2 >, \quad \text{(III.8)}$$

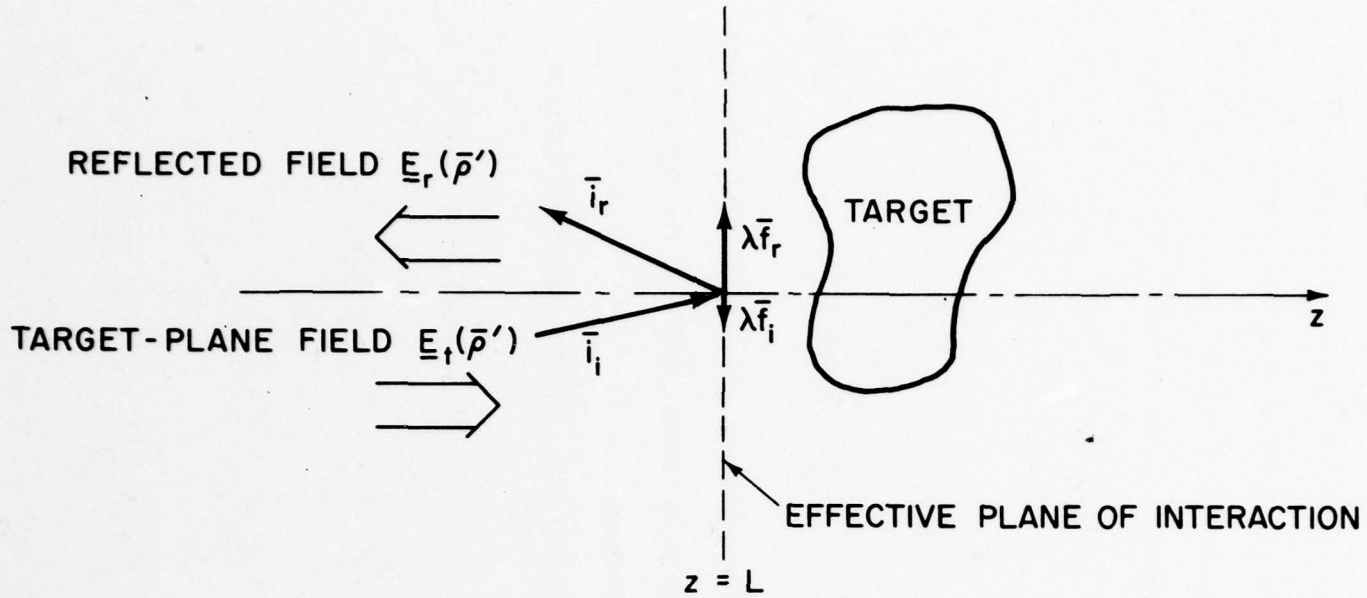

Fig. 8. Geometry for defining bidirectional reflectance $\rho'(\lambda;\bar{f}_i;\bar{f}_r)$; the target-plane field is chosen to be a plane wave of wavelength λ propagating in the direction of the unit vector $\bar{i}_i$ ($\lambda\bar{f}_i$ is the projection of $\bar{i}_i$ on the z = L plane); the radiance of the reflected field is measured in the direction of the unit vector $\bar{i}_r$ ($\lambda\bar{f}_r$ is the projection of $\bar{i}_r$ on the z = L plane).

where A_T is the target's projected area. In this figure, a target with reflection coefficient $\underline{T}(\bar{\rho}')$ at wavelength λ is illuminated by a plane wave $\underline{E}_t(\bar{\rho}') = \exp(j2\pi\ \bar{f}_i \cdot \bar{\rho}')$ at this wavelength, where $\bar{f}_i = \lambda^{-1} \sin\theta_i \times (\cos\phi_i, \sin\phi_i)$ gives the polar and azimuthal angles of incidence. The bi-directional reflectance therefore gives the ratio of the average reflected radiance (W/m^2SR) in the direction $\bar{f}_r = \lambda^{-1} \sin\theta_r\ (\cos\phi_r, \sin\phi_r)$ to the incident irradiance (W/m^2). Equations (III.4)-(III.8) yield

$$\rho'(\lambda;\ \bar{f}_i;\ \bar{f}_r) = A_T^{-1} \int d\bar{\rho}'\ T_s(\bar{\rho}')$$

$$+(\lambda^2 A_T)^{-1} \int d\bar{\rho}_1' \int d\bar{\rho}_2'\ \underline{T}_g(\bar{\rho}_1')\underline{T}_g^*(\bar{\rho}_2')\exp[j2\pi(\bar{f}_i-\bar{f}_r)\cdot(\bar{\rho}_1'-\bar{\rho}_2')]. \quad \text{(III.9)}$$

Note from (III.9) that the speckle and glint reflection components combine additively in bidirectional reflectance, and that the speckle contribution has no directionality whatsoever.

The glint contribution to $\rho'(\lambda;\ \bar{f}_i;\ \bar{f}_r)$ can be written as

$$(\lambda^2 A_T)^{-1} \int d\bar{\rho}_1' \int d\bar{\rho}_2'\ \underline{T}_g(\bar{\rho}_1')\ \underline{T}_g^*(\bar{\rho}_2')\exp[j2\pi(\bar{f}_i-\bar{f}_r)\cdot(\bar{\rho}_1'-\bar{\rho}_2')]$$

$$= (\lambda^2 A_T)^{-1} \int d\bar{\rho}'\ R_{gg}(\bar{\rho}')\exp[j2\pi(\bar{f}_i-\bar{f}_r)\cdot\bar{\rho}']$$

$$= (\lambda^2 A_T)^{-1}\ S_{gg}(\bar{f}_r - \bar{f}_i), \quad \text{(III.10)}$$

where

$$R_{gg}(\bar{\rho}') \equiv \int d\bar{\rho}_1'\ \underline{T}_g(\bar{\rho}_1' + \bar{\rho}'/2)\ \underline{T}_g^*(\bar{\rho}_1' - \bar{\rho}'/2)$$

is the spatial autocorrelation integral of $\underline{T}_g$, and

$$S_{gg}(\bar{f}) \equiv \int d\bar{\rho}' \, R_{gg}(\bar{\rho}') \exp(-j2\pi \, \bar{f} \cdot \bar{\rho}')$$

is the spatial spectrum of $\underline{T}_g$ (the Fourier transform of R_{gg}). Evidently, in our model, the directionality properties of $\rho'(\lambda; \bar{f}_i; \bar{f}_r)$ are directly attributable to the spatial spectrum of the glint reflection component.

IV. IMAGE SIGNAL-TO-NOISE RATIO

We shall now bring the extended Huygens-Fresnel principle atmospheric propagation model, and the planar target-reflection model to bear on evaluating the performance of a CO_2 laser heterodyne reception imaging radar.

Consider the use of the radar configuration described in Section I.1 to image a target at range L. Specifically, let us assume that a single pulse is transmitted with spatial mode

$$\underline{\xi}_T(\bar{\rho}) = (4/\pi d^2)^{1/2} \exp(j2\pi \bar{f}_T \cdot \bar{\rho}), \text{ for } |\bar{\rho}| \leq d/2 \qquad \text{(IV.1)}$$

i.e., the transmitter radiates a collimated beam which propagates in the direction of the unit vector

$$\bar{i}_T = [2\pi \bar{f}_T + (k^2 - |2\pi \bar{f}_T|^2)^{1/2} \, \bar{i}_z]/k$$

where $\bar{i}_z$ is a +z directed unit vector. For $d^2/\lambda L < 1$, $d < \rho_o$, as will almost always be the case for target ranges of interest, far-field propagation prevails with no turbulence-induced beam spreading. The target-plane field, $\underline{E}_t(\bar{\rho}')$, therefore satisfies (II.12) with

$$\underline{\xi}_t(\bar{\rho}') \approx (\pi d^2/4)^{1/2}\ (j\lambda L)^{-1}\ \exp(jkL + jk|\bar{\rho}'|^2/2L)$$

$$\times\ J_1(\pi d|\bar{\rho}' - \lambda L\bar{f}_T|/\lambda L)/(\pi d|\bar{\rho}' - \lambda L\bar{f}_T|/2\lambda L). \qquad \text{(IV.2)}$$

Thus, the radar illuminates a nominal $\lambda L/d$ diameter region of the target centered on the point $\bar{\rho}' = \lambda L\bar{f}_T$. We shall assume perfect transmitter local oscillator mode-matching has been achieved, i.e., $\underline{\xi}_\ell(\bar{\rho}) = \underline{\xi}_T^*(\bar{\rho})$, and, because $d < \rho_o$ has already been assumed, we have that the receiver's IF envelope, $\underline{r}(t)$, satisfies (I.8) with

$$(c\varepsilon_o/2)^{1/2} \int d\bar{\rho}\ \underline{E}_R(\bar{\rho})\ \underline{\xi}_\ell{}^*(\bar{\rho}) \approx$$

$$P_T{}^{1/2} \int d\bar{\rho}'\ \underline{\xi}_t{}^2(\bar{\rho}')\ \underline{T}(\bar{\rho}')\ \exp\ (2\chi(\bar{\rho}', \bar{0}) + 2j\phi(\bar{\rho}', \bar{0})). \qquad \text{(IV.3)}$$

Equation (IV.3) has the merit of representing the signal component of the IF envelope $\underline{r}(t)$ directly in terms of a target-plane integral. This integral contains the interaction between the free-space radar beam pattern $\underline{\xi}_t(\bar{\rho}')$, the target's reflection coefficient $\underline{T}(\bar{\rho}')$, and the turbulence-induced propagation perturbations $\exp\ (2\chi(\bar{\rho}', \bar{0}) + 2j\phi(\bar{\rho}', \bar{0}))$.

IV.1 SNR Analysis

Image SNR analysis can now proceed rapidly. The radar receiver's IF envelope $\underline{r}(t)$ consists of the signal term (IV.3), plus a statistically independent zero-mean circulo-complex Gaussian noise process with power spectral density (I.9). It is essentially straightforward to compute the

mean and variance of the matched-filter envelope detector output. For simplicity, we shall take $W = 1/t_p$, so that the IF filter itself serves as the matched filter and

$$|t_p^{-1} \int_0^{t_p} \underline{r}(t)\, dt|^2 \approx |\underline{r}(0)|^2.$$

With this simplification we find that

$$\langle|\underline{r}(0)|^2\rangle = \langle|\underline{Y}|^2\rangle + 2h\nu_o\, W/\eta \qquad \text{(IV.4)}$$

and

$$\text{Var}\,(|\underline{r}(0)|^2) = \text{Var}\,(|\underline{Y}|^2) + 4\langle|\underline{Y}|^2\rangle h\nu_o\, W/\eta + (2h\nu_o\, W/\eta)^2, \qquad \text{(IV.5)}$$

are the mean value and variance of the matched-filter envelope detector output where

$$\underline{Y} \equiv P_T^{1/2} \int d\bar{\rho}'\, \underline{\xi}_t^2(\bar{\rho}')\, \underline{T}(\bar{\rho}')\, \exp(2\chi(\bar{\rho}', \bar{0}) + 2j\phi(\bar{\rho}', \bar{0})),$$

and expectations have been taken over the turbulence, target, and receiver-noise ensembles. Because the $2h\nu_o\, W/\eta$ term in (IV.4) corresponds to a constant target-independent level (which is due physically to receiver noise) we define the image SNR to be

$$\text{SNR} = \frac{(\langle|\underline{r}(0)|^2\rangle - 2h\nu_o\, W/\eta)^2}{\text{Var}\,(|\underline{r}(0)|^2)} \qquad \text{(IV.6)}$$

From (IV.4), (IV.5) we find

$$SNR = \frac{(<|\underline{y}|^2>)^2}{Var\ (|\underline{y}|^2) + 4\ <|y|^2>\ h\nu_o\ W/\eta + (2h\nu_o\ W/\eta)^2}$$

$$= \frac{CNR/2}{1 + CNR\ Var\ (|\underline{y}|^2)/2\ <|\underline{y}|^2>^2 + (2CNR)^{-1}} \qquad (IV.7)$$

where the carrier-to-noise ratio (CNR)

$$CNR = <|\underline{y}|^2> / (2h\nu_o\ W/\eta) \qquad (IV.8)$$

is the ratio of the mean signal and mean noise contributions to $|\underline{r}(0)|^2$.

The three terms in the denominator of (IV.7) represent, physically, the fluctuations in $|\underline{r}(0)|^2$ that are due, respectively, to signal x noise fluctuations, signal x signal fluctuations, and noise x noise fluctuations. In the absence of turbulence and target fluctuations, we have the Var $(|\underline{y}|^2)$ = 0 (see below); at high CNR values we then find SNR $\tilde{\approx}$ CNR / 2. For CNR $\geq$ 5 the noise x noise term in the denominator of (IV.7) becomes insignificant and we can use

$$SNR \tilde{\approx} \frac{CNR/2}{1 + CNR\ Var\ (|\underline{y}|^2)/2\ <|\underline{y}|^2>^2}, \qquad (IV.9)$$

which is equivalent to the universal curve

$$\frac{SNR}{SNR_{SAT}} \tilde{\approx} \frac{CNR\ /\ 2\ SNR_{SAT}}{1 + CNR\ /\ 2\ SNR_{SAT}}, \qquad (IV.10)$$

in terms of a saturation signal-to-noise ratio

$$SNR_{SAT} \equiv \langle|\underline{Y}|^2\rangle^2/\text{Var}\ (|\underline{Y}|^2). \tag{IV.11}$$

Equation (IV.10) has been plotted in Fig. 9; evidently increasing CNR beyond $2SNR_{SAT}$ does little to improve image signal-to-noise ratio.

The preceding discussion implies that we should focus our attention on evaluating CNR and SNR_{SAT} for various target and turbulence conditions. To do this we must find $\langle|\underline{Y}|^2\rangle$ and Var $(|\underline{Y}|^2)$.

Using the results of Sections II and III we find that

$$\begin{aligned}
\langle|\underline{Y}|^2\rangle &= P_T\,\lambda^2\, e^{4\sigma_\chi^2} \int d\bar{\rho}'\ |\underline{\xi}_t^2(\bar{\rho}')|^2\ T_s(\bar{\rho}') \\
&+ P_T\, e^{4\sigma_\chi^2} \int d\bar{\rho}_1' \int d\bar{\rho}_2'\ \underline{\xi}_t^2(\bar{\rho}_1')\ \underline{\xi}_t^{*2}(\bar{\rho}_2')\ \underline{T}_g(\bar{\rho}_1')\ \underline{T}_g^*(\bar{\rho}_2') \\
&\qquad \times \exp\left(-2\, D(\bar{\rho}_1' - \bar{\rho}_2', \bar{0})\right) \\
&= P_T\, e^{4\sigma_\chi^2}\ [\lambda^2 \int d\bar{\rho}'\ |\underline{\xi}_t^2(\bar{\rho}')|^2\ T_s(\bar{\rho}') \\
&+ \int d\bar{\rho}'\ R_{gg}'(\bar{\rho}')\ \exp[-2(|\bar{\rho}'|\ /\ \rho_o')^{5/3}]]
\end{aligned} \tag{IV.12}$$

where, in the second equality, R_{gg}' is the spatial autocorrelation integral of $\underline{\xi}_t^2\ \underline{T}_g$ (cf. (III.10)) and $\rho_o' \equiv [2.91\ k^2 \int_0^L dz\ C_n^2(z)(z/L)^{5/3}]^{-3/5}$ is the turbulence field coherence length in the target plane (cf. (II.11)). Equation (IV.12) applies to an arbitrary target (polished, rough, or semi-rough) and arbitrary turbulence levels (up to the point $d = \rho_o$).

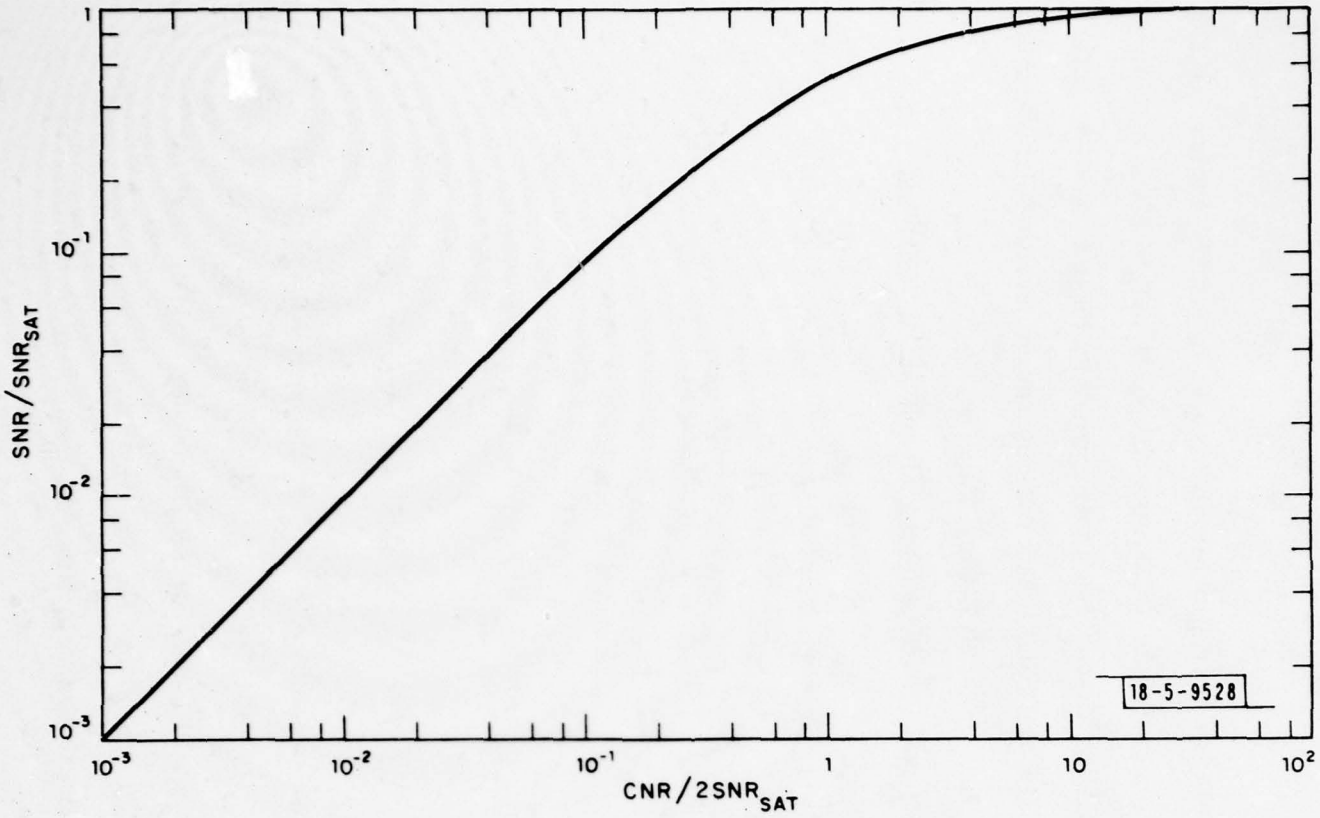

Fig. 9. Universal curve for normalized image signal-to-noise ratio vs normalized carrier-to-noise ratio, Eq.(IV.10).

Weak perturbation turbulence theory can be used, in conjunction with our target model, to obtain a general expression for Var $(|\underline{\gamma}|^2)$. We shall not produce such an expression; it is near-hopeless in its complication. Instead, we shall develop from (IV.12) simpler results for $\langle|\underline{\gamma}|^2\rangle$ and Var $(|\underline{\gamma}|^2)$ when the target has but a single glint (in addition to its speckle component).

IV.2 The Single-Glint Approximation

Consider the spatial autocorrelation integral

$$R'_{gg}(\bar{\rho}') = \int d\bar{\rho}_1' \; \underline{\xi}_t^2(\bar{\rho}_1' + \bar{\rho}'/2) \; \underline{T}_g(\bar{\rho}_1' + \bar{\rho}'/2)$$

$$\times \; \underline{\xi}_t^{*2}(\bar{\rho}_1' - \bar{\rho}'/2) \; \underline{T}_g^*(\bar{\rho}_1' - \bar{\rho}'/2), \qquad \text{(IV.13)}$$

which enters into (IV.12). Because $|\underline{\xi}_t(\bar{\rho}')|^2 \approx 0$ for $|\bar{\rho}' - \lambda L\bar{f}_T| \gtrsim \lambda L/2d$ (recall (IV.2)), $|R'_{gg}(\bar{\rho}')| \approx 0$ for $|\bar{\rho}'| \gtrsim \lambda L/d$. Thus, if $\lambda L/d \lesssim \rho_o'/2$ then the glint contribution to $\langle|\underline{\gamma}|^2\rangle$ satisfies

$$\int d\bar{\rho}' \; R'_{gg}(\bar{\rho}') \exp[-2(|\bar{\rho}'|/\rho_o')^{5/3}] \approx \int d\bar{\rho}' \; R'_{gg}(\bar{\rho}'), \qquad \text{(IV.14)}$$

i.e., the turbulence causes no beam spreading of the glint return. Unfortunately, $\lambda L/d \lesssim \rho_o'/2$ is an unduly restrictive condition, viz, it is violated for a variety of d, L, C_n^2 values of interest. A more careful examination of $R'_{gg}(\bar{\rho}')$ reveals that there is a much weaker condition which permits us to use (IV.14). Indeed, this condition, developed below, permits a useful simplification of the glint contribution to $\underline{\gamma}$ itself, before ensemble averaging.

Suppose $\underline{T}_g(\bar{\rho}')$ is given by

$$\underline{T}_g(\bar{\rho}') \approx \Gamma^{1/2} \exp(-jk|\bar{\rho}' - \bar{\rho}'_c|^2/R_c) \qquad \text{(IV.15)}$$

for $|\bar{\rho}' - \lambda L \bar{f}_T| \lesssim \lambda L/2d$, i.e., the glint reflection behaves like a spherical reflector over the region illuminated by the radar. Assuming $R_c << L$ (which should often if not always be the case), (IV.15) implies that $|R'_{gg}(\bar{\rho}')| \approx 0$ for $|\bar{\rho}'| \gtrsim \frac{dR_c}{L}$. It then follows that (IV.14) may be employed because $d < \rho_o$, $R_c << L$ have been assumed and $\rho_o \approx \rho_o'$ for horizontal or near-horizontal paths (uniform C_n^2 profiles).

We can show, by direct consideration of

$$P_T^{1/2} \int d\bar{\rho}' \, \underline{\xi}_t^2(\bar{\rho}') \, \underline{T}_g(\bar{\rho}') \exp(2\chi(\bar{\rho}', \bar{0}) + 2j\phi(\bar{\rho}', 0) + j\theta)$$

which is the glint contribution to $\underline{y}$, that when (IV.15) is satisfied, only a region of nominal diameter $(\lambda R_c)^{1/2}$ within the illuminated portion of the target makes an appreciable contribution. This is the stationary-phase region [33] on the target; it is the Fresnel zone of the curvature R_c centered on the reflection point which produces a wavefront directed towards the radar receiver when illuminated by $\underline{\xi}_t(\bar{\rho}')$, see Fig. 10. For reasonable R_c values $(\lambda R_c)^{1/2} < \rho_o'$ can be assumed hence

$$P_T^{1/2} \int d\bar{\rho}' \, \underline{\xi}_t^2(\bar{\rho}') \, \underline{T}_g(\bar{\rho}') \exp(2\chi(\bar{\rho}', \bar{0}) + 2j\phi(\bar{\rho}', \bar{0}) + j\theta)$$

$$\approx P_T^{1/2} \int d\bar{\rho}' \, \underline{\xi}_t^2(\bar{\rho}') \, \underline{T}_g(\bar{\rho}') \exp(2\chi(\bar{\rho}'_g, \bar{0}) + 2j\phi(\bar{\rho}'_g, \bar{0}) + j\theta) \qquad \text{(IV.16)}$$

18-5-9266

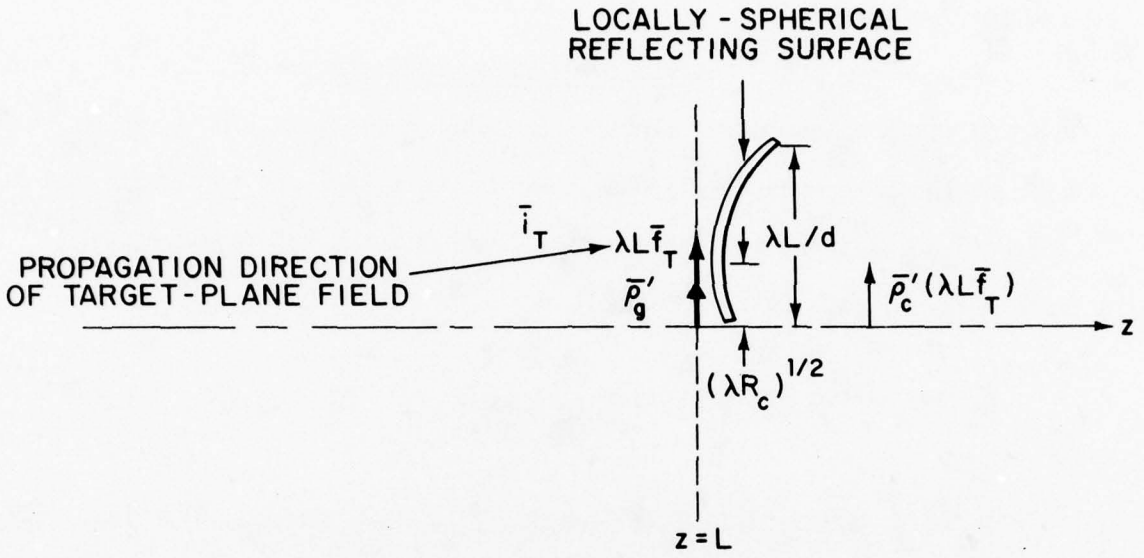

Fig. 10. Geometry for the single-glint approximation; the target-plane field has direction of propagation $\bar{i}_T$ and illuminates a region of the target with nominal diameter $\lambda L/d$ centered on the point $\lambda L \bar{f}_T$ in the z = L plane ($\lambda \bar{f}_T$ is the projection of $\bar{i}_T$ on the z = L plane); over this region the target is assumed to be a spherical reflector with center of curvature $\bar{\rho}_c'(\lambda L \bar{f}_T)$ and radius of curvature $R_c(\lambda L \bar{f}_T)$ ($R_c > 0$ is shown); the only appreciable contribution to the received field at z = 0 comes from a Fresnel-zone region (nominal radius $(\lambda R_c)^{1/2}$) about the glint reflection point $\bar{\rho}_g'$; $\bar{\rho}_g'$ is found by projecting $\bar{\rho}_c'(\lambda L \bar{f}_T)$ onto the z = L plane in the direction of $-\bar{i}_T$ for $R_c < 0$ and $\bar{i}_T$ for $R_c \geq 0$.

where $\bar{\rho}'_g$ is the glint reflection point. (Use of (IV.16) reproduces the weaker condition (IV.14), but the former has additional advantages in finding $\mathrm{Var}(|\underline{Y}|^2)$).

We can now state the single-glint approximation. If, for $|\bar{\rho}' - \lambda L\bar{f}_T| \lesssim \lambda L/2d$, $\underline{T}_g(\bar{\rho}')$ has only a single-stationary phase point for specular reflection of the beam mode $\underline{\xi}_t(\bar{\rho}')$ back towards the radar, and if the Fresnel zone (effective radiating region) for this point has nominal diameter $(\lambda R_c)^{1/2}$ with $R_c << L$, $(\lambda R_c)^{1/2} < \rho_o'$ then

$$\underline{Y} \approx P_T^{1/2} \int d\bar{\rho}'\ \underline{\xi}_t^2(\bar{\rho}')\ \underline{T}_s(\bar{\rho}')\ \exp(2\chi(\bar{\rho}', \bar{0}) + 2j\phi(\bar{\rho}', \bar{0}))$$

$$+ P_T^{1/2} \int d\bar{\rho}'\ \underline{\xi}_t^2(\bar{\rho}')\ \underline{T}_g(\bar{\rho}')\ \exp(2\chi(\bar{\rho}'_g, \bar{0}) + 2j\phi(\bar{\rho}'_g, \bar{0}) + j\theta), \quad \text{(IV.17)}$$

where $\bar{\rho}'_g$ is the glint reflection point, is the signal contribution to the receiver's IF complex envelope $\underline{r}(t)$.

From (IV.17), and the results of Sections II and III, we can show that

$$\langle|\underline{Y}|^2\rangle \approx P_T e^{4\sigma\chi^2} [\lambda^2 \int d\bar{\rho}'\ |\underline{\xi}_t^2(\bar{\rho}')|^2\ T_s(\bar{\rho}') + \int d\bar{\rho}'\ R'_{gg}(\bar{\rho}')]. \quad \text{(IV.18)}$$

For an object that lies entirely within the target-plane region illuminated by the radar, we have

$$R'_{gg}(\bar{\rho}') \approx |\underline{\xi}_t^2(\lambda L\bar{f}_T)|^2 \exp(j4\pi\bar{f}_T\cdot\bar{\rho}')\ R_{gg}(\bar{\rho}'), \quad \text{(IV.19)}$$

and the glint contribution to $\langle|\underline{y}|^2\rangle$ is directly related to the bidirectional reflectance. Using the weak-perturbation turbulence theory and the single-glint approximation we now get this "simple" expression for $\mathrm{Var}(|\underline{y}|^2)$

$$\mathrm{Var}\,(|\underline{y}|^2) \approx$$

$$\lambda^2 P_T^2 e^{8\sigma_\chi^2} \int d\bar{\rho}_1' \int d\bar{\rho}_2'\; T_s(\bar{\rho}_1')\, T_s(\bar{\rho}_2')\, |\underline{\xi}_t^2(\bar{\rho}_1')|^2$$

$$\times |\underline{\xi}_t^2(\bar{\rho}_2')|^2\, [2\exp(16\, C_{\chi\chi}(\bar{\rho}_1' - \bar{\rho}_2', \bar{0})) - 1]$$

$$+ 2\lambda^2 P_T^2 e^{8\sigma_\chi^2} \int d\bar{\rho}_1'\; T_s(\bar{\rho}_1')\, |\underline{\xi}_t^2(\bar{\rho}_1')|^2$$

$$\times [2\exp(16\, C_{\chi\chi}(\bar{\rho}_1' - \bar{\rho}_g', \bar{0})) - 1] \int d\bar{\rho}_2'\; R'_{gg}(\bar{\rho}_2')$$

$$+ P_T^2 e^{8\sigma_\chi^2} \left(\int d\bar{\rho}'\; R'_{gg}(\bar{\rho}') \right)^2 (e^{16\sigma_\chi^2} - 1) \qquad \text{(IV.20)}$$

Equations (IV.18), (IV.20) will be used henceforth; in conjunction with Equations (IV.7)-(IV.11) they complete the general SNR analysis for the imaging radar in the single-glint approximation.

IV.3 SNR Examples

To illustrate the interplay between receiver noise, turbulence-induced scintillation, and target speckle in determining image SNR, we shall consider a series of simple examples. At times, rather gross approximations will be made to arrive quickly at numerical results. These approximations, however, will not detract from our main purpose, viz, to gain an intuitive understanding of the various SNR degradations.

Case 1 No turbulence, specular target.

Consider the imaging of a specular target, i.e., one for which $\underline{T}(\bar{\rho}') = \underline{T}_g(\bar{\rho}')\, e^{j\theta}$, in the absence of turbulence. (This is the most favorable situation inasmuch as image signal-to-noise ratio will be limited only by receiver noise.) We have that the fundamental performance equations reduce to the following set for this case:

$$SNR^{\circ}_g = \frac{CNR^{\circ}_g /2}{1 + (2CNR^{\circ}_g)^{-2}} \tag{IV.21}$$

$$CNR^{\circ}_g = (\eta P_T/2h\nu_o W) \int d\bar{\rho}'\, R'_{gg}(\bar{\rho}'), \tag{IV.22}$$

where the superscript "o" denotes free space propagation and the subscript "g" denotes glint target.

For simplicity, in this example and those that follow we shall use (IV.19) for $R'_{gg}(\bar{\rho}')$, whence (with the aid of (III.10)) (IV.22) reduces to

$$CNR^{\circ}_g = (\eta P_T/2h\nu_o W)\ |\underline{\xi}_t{}^2(\lambda L\bar{f}_T)|^2\lambda^2 A_T\rho'(\lambda;\bar{f}_T;-\bar{f}_T). \tag{IV.23}$$

It is reassuring to see that our theory reduces to such an intuitively obvious result. Equation (IV.23) shows that the no-turbulence no-speckle carrier-to-noise ratio (for a target smaller than the radar beam size) equals the on-target irradiance, $P_T\ |\underline{\xi}_t(\lambda L\bar{f}_T)|^2$, times the bidirectional reflectance for specular reflection back towards the radar $\rho'(\lambda;\bar{f}_T;-\bar{f}_T)$, times the target's area, A_T, times the heterodyne receiver's antenna gain,

$\lambda^2 |\underline{\xi}_t(\lambda L \bar{f}_T)|^2$, divided by the local-oscillator shot noise power in the IF bandwidth, $2h\nu_o W/\eta$.

Equation (IV.23) is plotted in Figure 11 vs. path length L, assuming the parameter values given in Table 2. Because the extended Huygen-Fresnel principle we have employed neglects absorption, (IV.23) is optimistic. We can correct for absorption in all of our signal-to-noise, carrier-to-noise results by replacing P_T by $P_T \exp(-2\,\alpha\, L)$ where α is the 10.6μm absorption coefficient; two such absorption-corrected CNR°_g curves are included in Fig. 11. Inasmuch as $CNR^\circ_g \geq 5$ will prevail under the conditions assumed in Fig. 11 we may use $SNR^\circ_g \approx CNR^\circ_g/2$ in lieu of (IV.21). Note that this corresponds to a curve of the form (IV.10), with a free-space propagation/glint target saturation signal-to-noise ratio $SNR^\circ_{gSAT} = \infty$, as expected from (IV.11) with $Var(|\underline{y}|^2) = 0$.

Case 2 No turbulence, diffuse target

In the absence of turbulence with $\underline{T}(\bar{\rho}') = \underline{T}_s(\bar{\rho}')$, we obtain the image signal-to-noise ratio

$$SNR^\circ_s = \frac{CNR^\circ_s/2}{1 + CNR^\circ_s/2 + (2CNR^\circ_s)^{-1}} \qquad \text{(IV.24)}$$

where

$$CNR^\circ_s = (\eta P_T/2h\nu_o W)\, \lambda^2 \int d\bar{\rho}'\, |\underline{\xi}_t{}^2(\bar{\rho}')|^2\, T_s(\bar{\rho}'), \qquad \text{(IV.25)}$$

and the subscript "s" denotes speckle target. It follows from (IV.24) that SNR°_s increases monotonically with increasing CNR°_s. When $CNR^\circ_s \geq 5$,

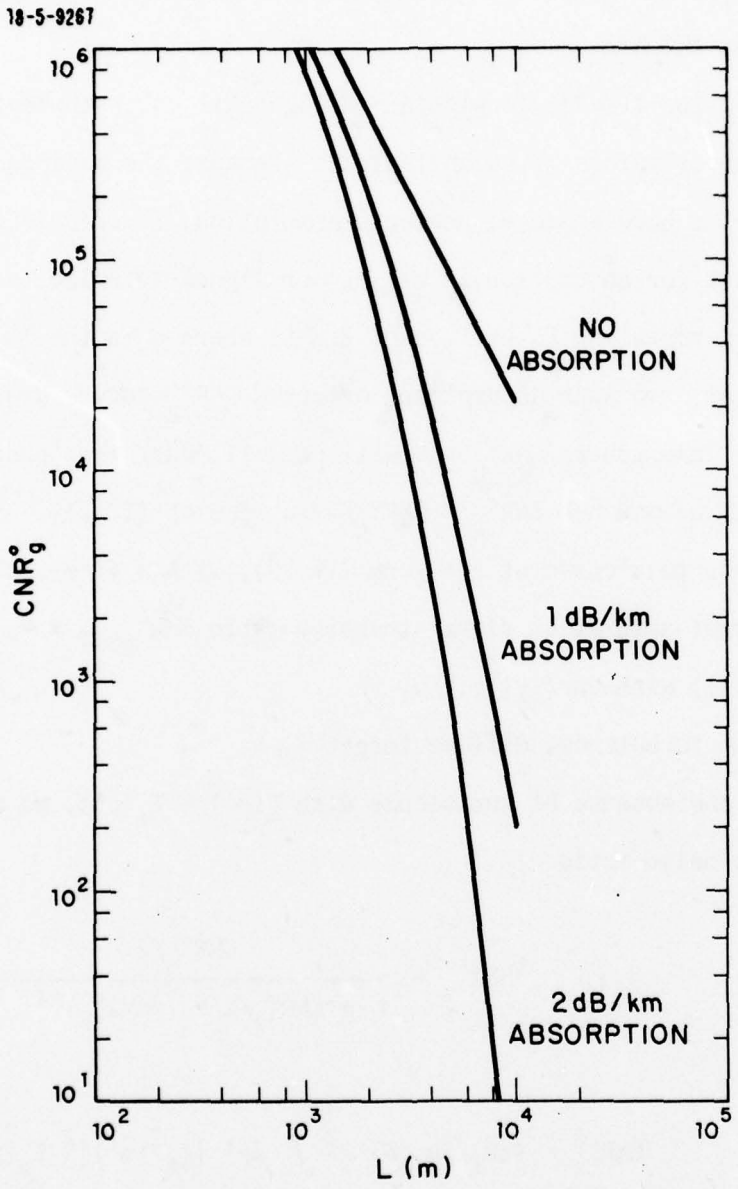

Fig. 11. Free-space carrier-to-noise ratio vs path length L for a pure glint target; Eq.(IV.23) is used with system parameters as given in Table 2.

TABLE 2

PARAMETER VALUES FOR $CNR°_g$ EVALUATION

TRANSMITTER PEAK POWER $P_T = 10^3 W$

DETECTOR QUANTUM EFFICIENCY $\eta = 0.2$

TRANSMITTER/RECEIVER PUPIL DIAMETER $d = 0.1$ m

UNILATERAL IF BANDWIDTH $2W = 2.0 \times 10^7$ Hz

CO_2 LASER PHOTON ENERGY $h\nu_o = 1.87 \times 10^{-20}$ J

GLINT BIDIRECTIONAL REFLECTANCE (see [2, Fig. 16])

$$\rho'(\lambda; \bar{f}_T; -\bar{f}_T) = 0.5 \text{ SR}^{-1}$$

TARGET AREA $A_T = 4(\lambda L/d)^2/\pi$

ABSORPTION COEFFICIENTS (see [2, TABLE 2])

$\alpha = 0$ (NO ABSORPTION)

$\alpha = 0.23 \text{ km}^{-1}$ (1 dB/km)

$\alpha = 0.46 \text{ km}^{-1}$ (2 dB/km)

however, Eq. (IV.24) can be replaced with

$$SNR^{\circ}_{s} = \frac{CNR^{\circ}_{s}\ /2}{1 + CNR^{\circ}_{s}\ /\ 2} \qquad \text{(IV.26)}$$

which is of the form (IV.10) with a free-space propagation/speckle target saturation signal-to-noise ratio $SNR^{\circ}_{s\ SAT} = 1$. Thus, in the limit $CNR^{\circ}_{s} >> 1$, we find $SNR^{\circ}_{s} \approx 1$, which is the well known unity signal-to-noise ratio of laser speckle [11], [12]. Multiframe averaging is needed to overcome this speckle-induced performance limit.

Assuming here and in subsequent examples that $T_s(\bar{\rho}')$ does not vary appreciably over the target region illuminated by the radar, (IV.25) becomes

$$CNR^{\circ}_{s} \approx (\eta P_T/2h\nu_o W)\ \lambda^2\ T_s(\lambda L\bar{f}_T) \int d\bar{\rho}'\ |\underline{\xi}_t{}^2(\bar{\rho}')|^2$$

$$\approx (\eta P_T/2h\nu_o W)\ (d/L)^2\ T_s(\lambda L\bar{f}_T). \qquad \text{(IV.27)}$$

Equation (IV.27) has been plotted vs. path length in Figure 12, using $T_s = 0.1$ and other parameters as in Table 2. (We have also included in Figure 12, CNR°_{s} plots for two representative values of absorption coefficient.) For this example, $CNR^{\circ}_{s} >> 1$ will prevail (except for the case of 2dB/km absorption at path lengths in excess of 6 km), so that image signal-to-noise will indeed be speckle limited.

Case 3 No turbulence, semi-rough target

In the absence of turbulence with a semi-rough target, image signal-to-noise ratio satisfies

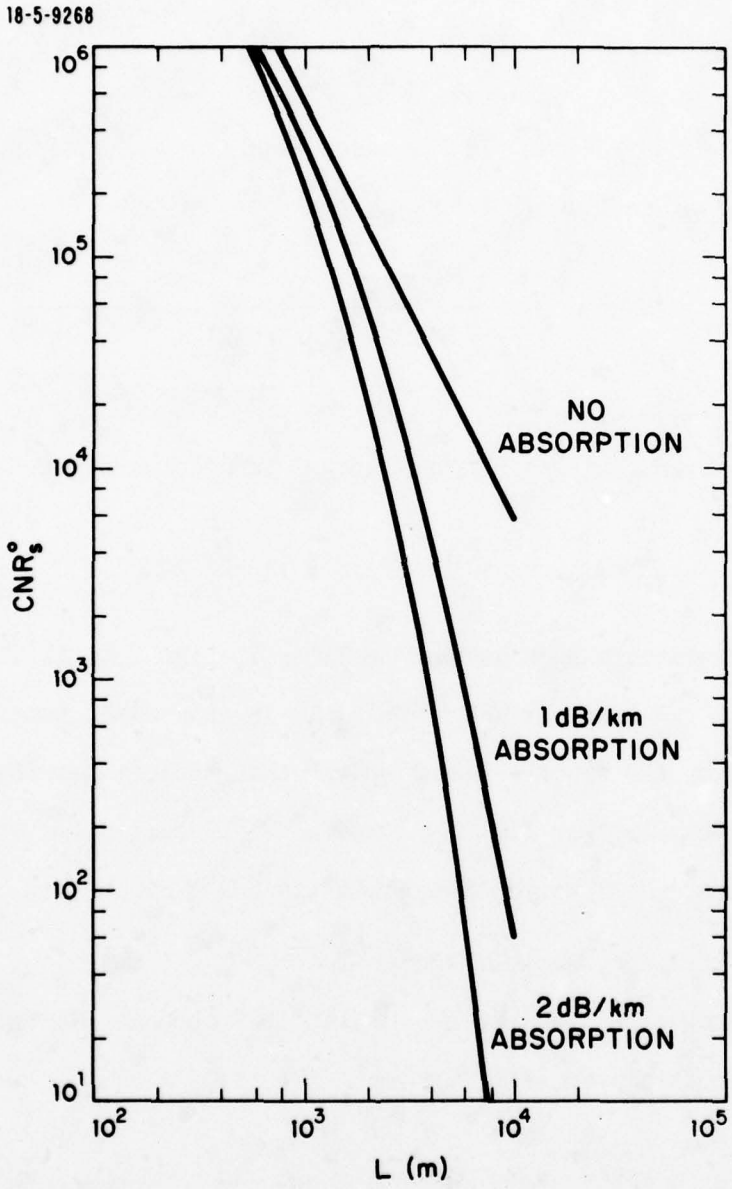

Fig. 12. Free-space carrier-to-noise ratio vs path length L for a pure diffuse target; Eq.(IV.27) is used with T_s = 0.1 and other parameters as in Table 2.

$$SNR^\circ = \frac{CNR^\circ/2}{1 + CNR^\circ_s/2 + (2CNR^\circ)^{-1}} \qquad (IV.28)$$

where $CNR^\circ = CNR^\circ_g + CNR^\circ_s$. For the parameters used in Figures 11, 12 we have $CNR^\circ \geq 5$, so that (IV.28) can be reduced to

$$SNR^\circ = \frac{CNR^\circ/2}{1 + CNR^\circ/2\ (CNR^\circ/CNR^\circ_s)} \qquad (IV.29)$$

Equation (IV.29) can be put in the standard form (IV.10) by identifying the free-space propagation/semi-rough target saturation signal-to-noise ratio

$$SNR^\circ_{SAT} = CNR^\circ/CNR^\circ_s = 1 + CNR^\circ_g/CNR^\circ_s. \qquad (IV.30)$$

For the parameter values assumed in Table 2, Figs. 11, 12 tell us that $CNR^\circ_g > CNR^\circ_s \geq 5$ hence $SNR^\circ \approx SNR^\circ_{SAT}$. In this case, image signal-to-noise is limited by the speckle-image "noise" that appears superimposed on the specular image. Other limiting cases of (IV.29) are also possible, e.g., $CNR^\circ_s >> CNR^\circ_g >> 1$ which reduces SNR° to SNR°_s etc.

Case 4 Turbulence, specular target

In imaging a specular target through turbulence we find that image signal-to-noise ratio satisfies

$$SNR_g = \frac{CNR_g/2}{1 + CNR_g(e^{16\sigma_\chi^2} - 1)/2 + (2CNR_g)^{-1}} \qquad (IV.31)$$

where $CNR_g = CNR^\circ_g\, e^{4\sigma_\chi^2}$. Assuming $CNR_g \geq 5$, (IV.31) takes the standard form

$$SNR_g = \frac{CNR_g/2}{1 + CNR_g/2SNR_{gSAT}}, \qquad (IV.32)$$

with

$$SNR_{gSAT} = (e^{16\sigma_\chi^2} - 1)^{-1}. \qquad (IV.33)$$

We see that for $\sigma_\chi^2 > 0$, SNR_g initially increases with increasing CNR_g, but reaches the scintillation-limited value (IV.33) once $CNR_g >> 2SNR_{gSAT}$. Evidently, turbulence-induced scintillation on a specular-target image is like the speckle fluctuations of the free-space image of a diffuse target, i.e., high carrier-to-noise ratio does not lead to high image signal-to-noise ratio. Multiframe averaging will be required to overcome this limit.

To gain some quantitative appreciation for the foregoing scintillation-limited signal-to-noise ratio, we have plotted SNR_{gSAT} vs. σ_χ^2 in Fig. 13, and σ_χ^2 vs. path length L (assuming a uniform C_n^2 profile) in Fig. 14. These figures show: for $L \sim 1$ km and realistic C_n^2 values (10^{-13} -10^{-16} $m^{-2/3}$) σ_χ^2 may range from less than 10^{-4} to in excess of 10^{-2}; σ_χ^2 values greater than 10^{-2} imply $SNR_{gSAT} \leq 60$.

Case 5 Turbulence, diffuse target

For a diffuse target, image signal-to-noise ratio in the presence of turbulence satisfies

$$SNR_s = \frac{CNR_s/2}{1 + CNR_s[1 + 2(e^{16\sigma_\chi^2} - 1)\zeta]/2 + (2CNR_s)^{-1}} \qquad (IV.34)$$

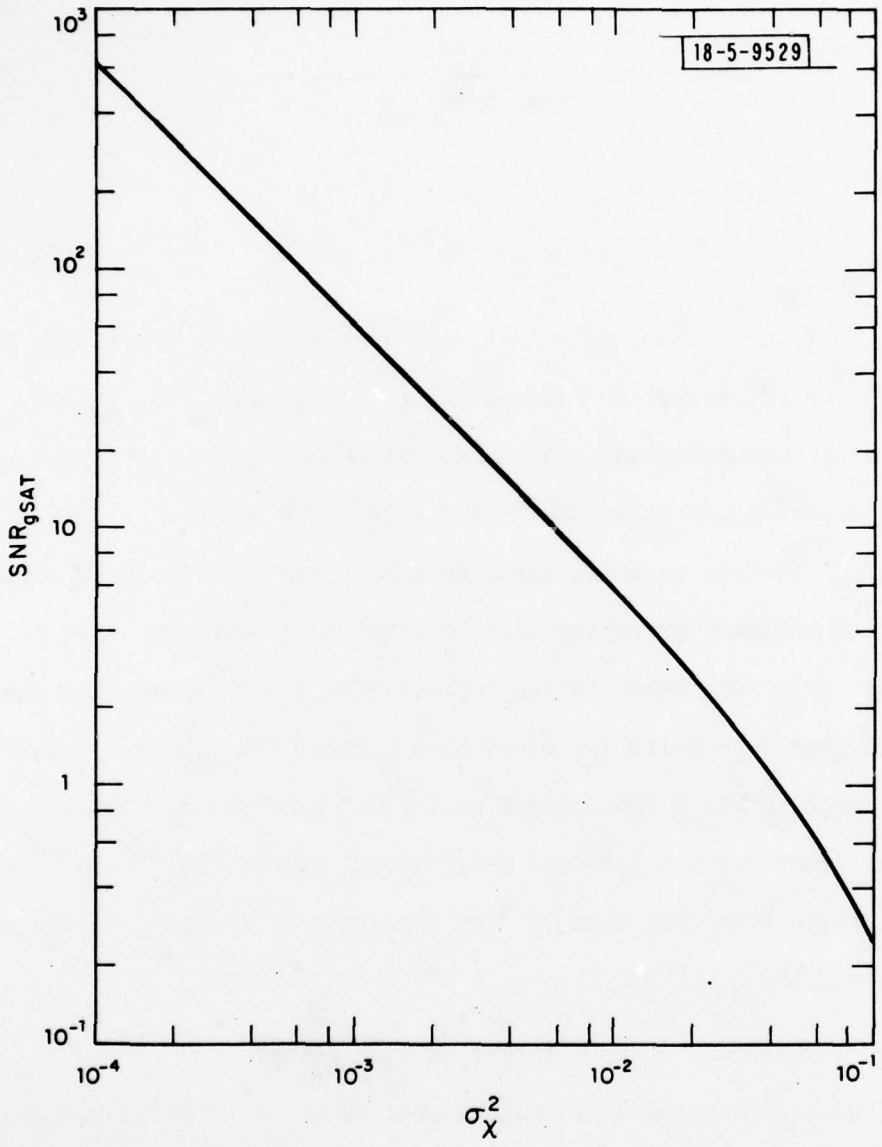

Fig. 13. Atmospheric propagation/glint target saturation signal-to-noise ratio SNR_{gSAT} vs log-amplitude variance σ_χ^2.

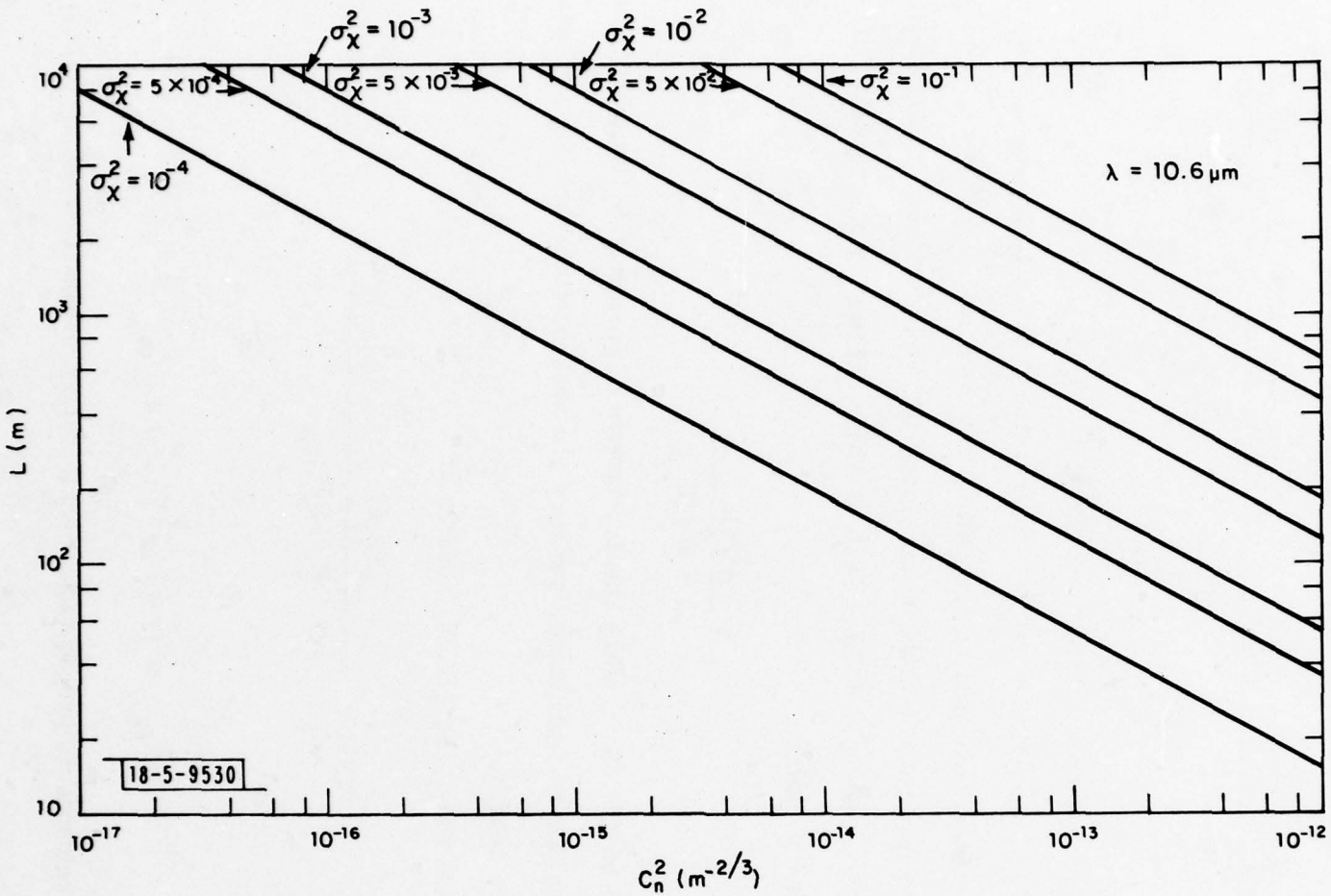

Fig. 14. Profiles of constant log-amplitude variance σ_χ^2 vs path length L and turbulence strength C_n^2; 10.6 μm wavelength is assumed.

In (IV.34), $CNR_s = CNR°_s\, e^{4\sigma_\chi^2}$ and

$$\zeta = \frac{\int d\bar{\rho}_1' \int d\bar{\rho}_2' \; |\underline{\xi}_t^2(\bar{\rho}_1')|^2 \; |\underline{\xi}_t^2(\bar{\rho}_2')|^2 [\exp(16\, C_{\chi\chi}(\bar{\rho}_1' - \bar{\rho}_2', \bar{0}) - 1]}{(e^{16\sigma_\chi^2} - 1) \left(\int d\bar{\rho}' \; |\underline{\xi}_t^2(\bar{\rho}')|^2 \right)^2} \tag{IV.35}$$

is the log-amplitude aperture averaging factor [7], [34]. It is easily shown that $\zeta \leq 1$. When $\lambda L/d < (\lambda L)^{1/2}$ so that the radar illuminates a single log-amplitude coherence area on the target plane we have $\zeta \approx 1$; when $\lambda L/d >> (\lambda L)^{1/2}$ we have approximately $\lambda L/d^2$ uncorrelated log-amplitude regions illuminated by the radar, whence $\zeta \approx d^2/\lambda L$. Both of these regimes can be conveniently summarized by using

$$\zeta \approx \frac{d^2/\lambda L}{1 + d^2/\lambda L} \tag{IV.36}$$

in place of (IV.35). (This result, remember, presumes no transmitter beam spreading due to turbulence, and uses the weak-perturbation log-amplitude coherence length.)

When $CNR_s \geq 5$, (IV.34) reduces to

$$SNR_s = \frac{CNR_s/2}{1 + CNR_s/2SNR_{sSAT}} \tag{IV.37}$$

where

$$SNR_{sSAT} = [1 + 2\,(e^{16\sigma_\chi^2} - 1)\zeta]^{-1} \tag{IV.38}$$

is the atmospheric propagation/speckle target saturation signal-to-noise ratio.

In Fig. 15 we have plotted SNR_{sSAT} vs. L for three representative C_n^2 values. These curves are obtained assuming a uniform C_n^2 distribution, d = 10 cm, and a target that fills the main lobe of the illuminator beam in the plane z = L; the curves are cut off at path lengths before saturation of scintillation is encountered. Note from Figure 15 that $SNR_{sSAT} \leq 1$; $SNR_{sSAT} = 1$ corresponds, physically to a signal-to-noise ratio limited by target speckle, the presence of strong turbulence ($C_n^2 = 10^{-12} m^{-2/3}$) or a long path length (L $\sim$ 10 km) with moderate turbulence ($C_n^2 = 10^{-14} m^{-2/3}$) may significantly reduce SNR_{sSAT} from the speckle-limited value of 1. To illustrate the aperture averaging effect in Figure 15, we have plotted ζ vs. L for d = 10 cm in Figure 16, assuming the target fills the main lobe of the illuminator beam. Without aperture averaging, the SNR_{sSAT} values in Figure 15 would be more than one order of magnitude <u>lower</u> at L = 10 km. In this regard, it is worth noting that targets which do not fill the main lobe of the illuminator beam do not achieve the full aperture averaging predicted by (IV.36).

V. RECEIVER OPERATING CHARACTERISTIC FOR TARGET DETECTION

The single-pulse target-detection problem for the CO_2 laser heterodyne reception optical radar is as follows. There are two possible hypotheses (target present or target absent at transverse coordinates $\bar{\rho}' = \lambda L \bar{f}_T$ in the plane z = L). If there is no target at $\bar{\rho}' = \lambda L \bar{f}_T$ in the z = L plane (hypothesis H_0), then the receiver's IF complex envelope, $\underline{r}(t)$, satisfies,

$$\underline{r}(t) = \underline{n}(t) \text{ for } 0 \leq t \leq t_p \qquad (V.1)$$

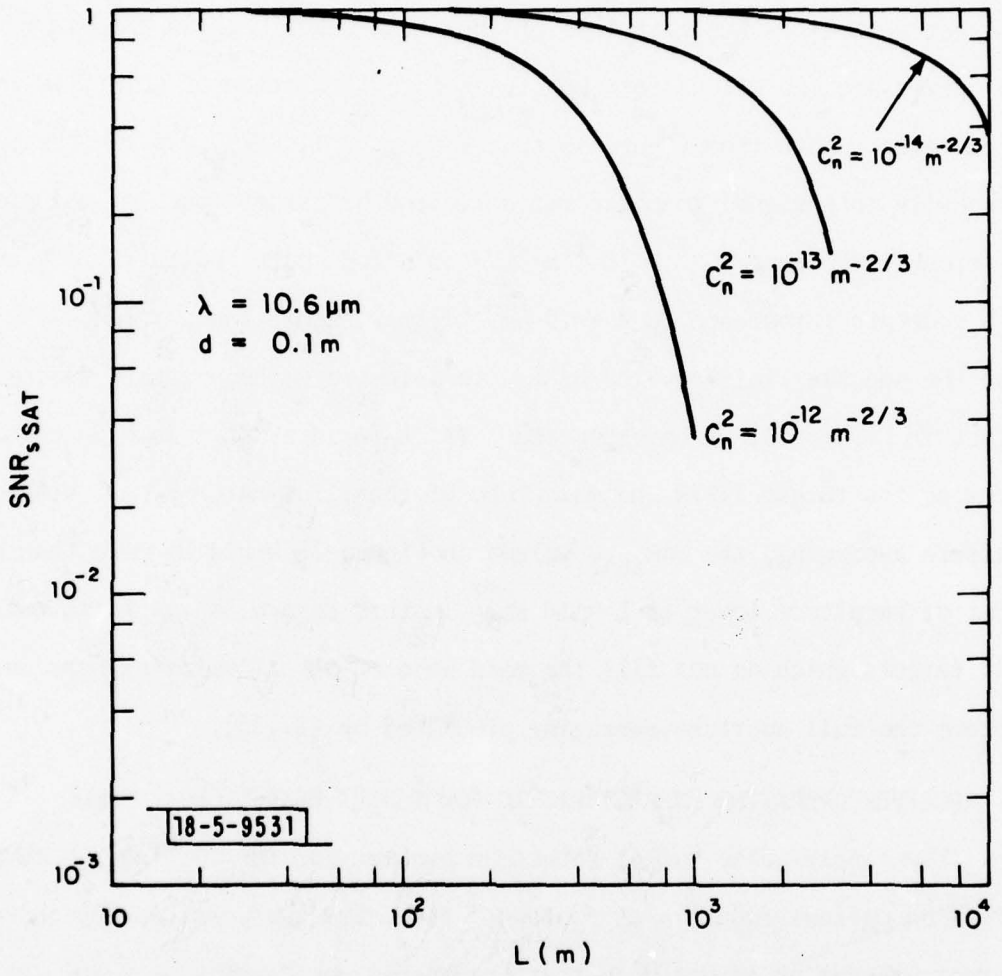

Fig. 15. Atmospheric propagation/speckle target saturation signal-to-noise ratio SNR_{sSAT} vs path length L for various turbulence-strength (C_n^2) values; 10.6 μm wavelength, d = 0.1 m, weak-perturbation propagation theory and a target area which fills the main lobe of the illuminator beam have been assumed.

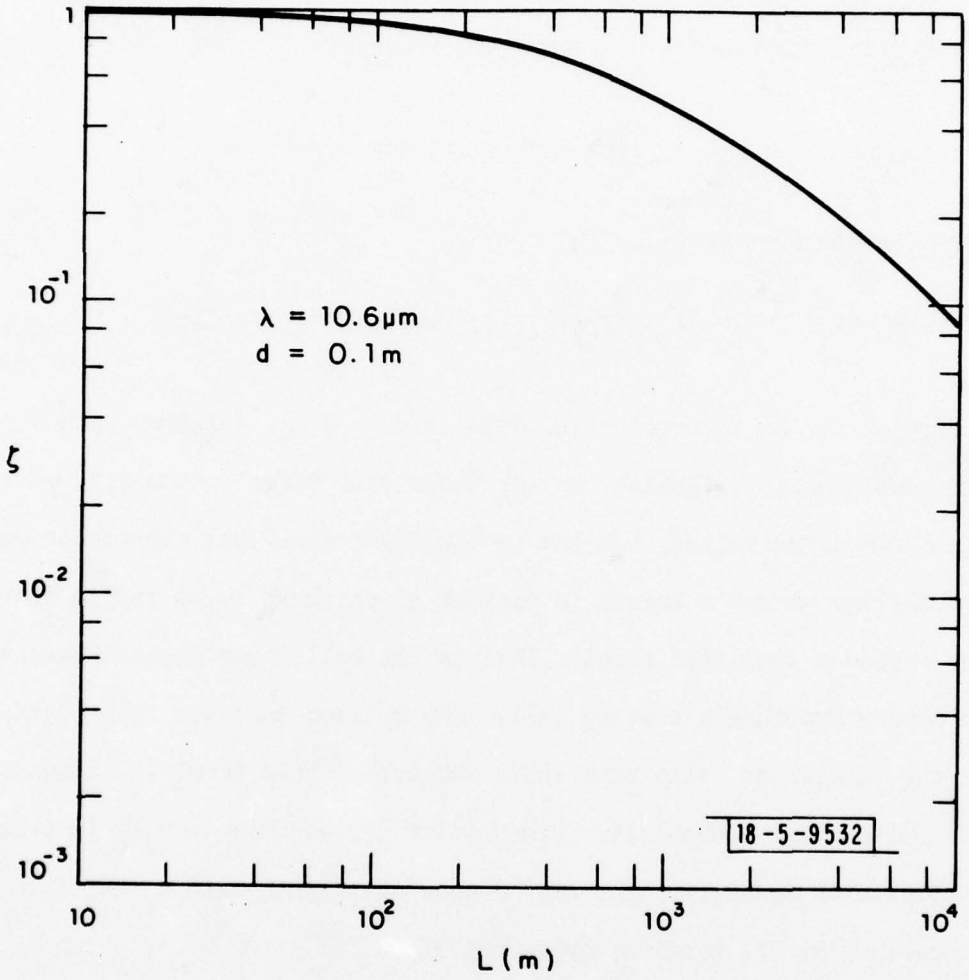

Fig. 16. Aperture averaging factor ζ vs path length L for a 10 cm pupil diameter at 10.6 μm wavelength.

where $\underline{n}(t)$ is the complex-Gaussian noise process with power spectrum (I.9) and $W \geq t_p^{-1}$ has been assumed. If there is a target at $\bar{\rho}' = \lambda L \bar{f}_T$ in the $z = L$ plane (hypothesis H_1), then the receiver's IF complex envelope obeys

$$\underline{r}(t) = \underline{\gamma} + \underline{n}(t) \text{ for } 0 \leq t \leq t_p \qquad (V.2)$$

where (as in Section IV)

$$\underline{\gamma} = P_T^{1/2} \int d\bar{\rho}' \, \underline{\xi}_t^2(\bar{\rho}') \, \underline{T}(\bar{\rho}') \exp(2\chi(\bar{\rho}', \bar{0}) + 2j\phi(\bar{\rho}', \bar{0})) \qquad (V.3)$$

Our objective is to process the data $\{\underline{r}(t) : 0 \leq t \leq t_p\}$ in such a way that the conditional probability we say there is a target present given there is one there is maximized, subject to the constraint that the conditional probability we say a target is present given there is no target there does not exceed a specified level. This is the well known Neyman-Pearson approach to binary hypothesis testing [35]. The optimum decision rule (data processor) is the likelihood ratio test (LRT) whose threshold level is chosen to satisfy the false-alarm probability (probability you say H_1 given H_0 is true) constraint with equality. The performance attainable with an LRT is conveniently summarized by its receiver operating characteristic (ROC), which is a parametric plot of the detection probability P_D (probability you say H_1 given H_1 is true) vs. the false-alarm probability P_F obtained by varying the threshold value.

V.1 The Likelihood-Ratio Test

The well known results for signal detection in additive white Gaussian

noise [36] permit us to express the LRT for the CO_2 radar in the following form when $W = 1/t_p$.

$$\int_0^\infty dY \int_0^{2\pi} d\phi \; Y \, p_{\underline{Y}}(\underline{Y}) \exp\left[\eta(\underline{r}(0)\underline{Y}^* - |\underline{Y}|^2/2)/h\nu_o W\right]$$

$$\begin{array}{l} \text{say } H_1 \\ \geq \\ < \\ \text{say } H_0 \end{array} \quad \tilde{\eta} \qquad \text{(V.4)}$$

where $Y \exp(j\phi)$ is the polar form of the complex number $\underline{Y}$, $p_{\underline{Y}}(\underline{Y})$ is the probability density for the complex random variable $\underline{Y}$, and $\tilde{\eta}$ is chosen to obtain a desired P_F level. The results of Sections II, III imply that

$$Y \, p_{\underline{Y}}(\underline{Y}) = p_y(y)/2\pi \text{ for } 0 \leq \phi \leq 2\pi \qquad \text{(V.5)}$$

where $p_y(Y)$ is the probability density for $y \equiv |\underline{Y}|$. Thus, the LRT (V.4) can be reduced to

$$\int_0^\infty dY \; p_y(Y) \; I_o(\eta|\underline{r}(0)|Y/h\nu_o W)\exp(-\eta Y^2/2h\nu_o W)$$

$$\begin{array}{l} \text{say } H_1 \\ \geq \\ < \\ \text{say } H_0 \end{array} \quad \tilde{\eta}, \qquad \text{(V.6)}$$

where I_o is the zeroth-order modified Bessel function [36]. Now, because I_o is a monotonically increasing function of its argument, the LRT (V.6) is equivalent to the threshold test

$$\begin{array}{c} \text{say } H_1 \\ \geq \\ |\underline{r}(0)|^2 \qquad\qquad \gamma \\ < \\ \text{say } H_0 \end{array} \qquad \text{(V.7)}$$

where γ is chosen to achieve the desired false-alarm probability. Because $W = t_p^{-1}$ has been assumed, (V.7) may be realized by matched-filter envelope detection followed by threshold comparison. Note that the optimality of the threshold test (V.7) applies regardless of the target character (specular, diffuse or semi-rough) and whether or not there is turbulence present along the propagation path. The performance of this test, viz, the ROC, is not similarly insensitive to the details of the problem. We shall investigate its behavior for specular and diffuse targets.

V.2 The Receiver Operating Characteristic

It turns out to be relatively easy to obtain the receiver operating characteristic for the threshold test (V.7) when the target is either specular or diffuse. Regardless of target and turbulence conditions, the IF complex envelope $\underline{r}(t)$ is pure receiver noise under hypothesis H_0. Thus for any target/turbulence combination we find that the false-alarm probability

is

$$P_F = \Pr\left[|\underline{n}(0)|^2 \geq \gamma\right] = \exp(-\eta\gamma/2h\nu_o W) \tag{V.8}$$

Equation (V.8) allows us to solve for the threshold level which gives false-alarm rate P_F, viz, the test

$$\begin{array}{c} \text{say } H_1 \\ \geq \\ |\underline{r}(0)|^2 \quad -(2h\nu_o W/\eta)\ln P_F \\ < \\ \text{say } H_0 \end{array} \tag{V.9}$$

has the maximum P_D-value attainable with false-alarm probability P_F. The detection probability is given by

$$P_D = \Pr\left[|\underline{y} + \underline{n}(0)|^2 \geq -(2h\nu_o W/\eta)\ln P_F\right]; \tag{V.10}$$

more explicit results are developed below.

Case 1 Specular Target

For a specular target in the single-glint approximation we have (cf. (IV.17))

$$\underline{y} \overset{\sim}{\sim} P_T^{1/2} \int d\bar{\rho}'\ \underline{\xi}_t^2(\bar{\rho}')\ \underline{T}_g(\bar{\rho}')\exp(2\chi(\bar{\rho}_g', \bar{0}) + 2j\phi(\bar{\rho}_g', \bar{0}) + j\theta) \tag{V.11}$$

Standard results from Gaussian detection theory [36] thus yield the conditional detection probability

$$\Pr\left[|\underline{Y} + \underline{n}(0)|^2 \geq -(2h\nu_o W/\eta)\ln P_F \mid |\underline{Y}| = Y\right]$$

$$= Q_M((\eta Y^2/h\nu_o W)^{1/2},\ (-2\ln P_F)^{1/2}), \qquad \text{(V.12)}$$

where

$$Q_M(\alpha,\beta) \equiv \int_\beta^\infty du\ u \exp\left[-(u^2+\alpha^2)/2\right] I_o(\alpha u)$$

is Marcum's Q-function [36]-[38]. It follows from (V.11) that $|\underline{Y}|$ is a lognormal random variable. Indeed, from Section IV, we have that

$$(\eta|\underline{Y}|^2/h\nu_o W)^{1/2} = (2CNR^\circ_g)^{1/2} \exp(2\chi(\bar{\rho}_g', \bar{0})). \qquad \text{(V.13)}$$

Because $\chi(\bar{\rho}_g', \bar{0})$ is a Gaussian random variable with mean $-\sigma_\chi^2$ and variance σ_χ^2, the detection probability is therefore

$$P_D = \int_{-\infty}^\infty d\chi\ p_\chi(\chi)\ Q_M((2CNR^\circ_g)^{1/2} e^{2\chi}, (-2\ln P_F)^{1/2}) \qquad \text{(V.14)}$$

where $p_\chi(\chi) = (2\pi\sigma_\chi^2)^{-1/2} \exp[-(\chi + \sigma_\chi^2)^2/2\sigma_\chi^2]$.

Despite the plethora of communication-theoretic calculations that are in the literature of optical propagation through turbulence, Eq. (V.14) has yet to be evaluated. Results for Marcum's Q-function are available [36]-[38], so that numerical values of the free-space detection probability (obtained by setting $\sigma_\chi^2 = 0$ in (V.14))

$$P_D^\circ = Q_M((2CNR^\circ_g)^{1/2},\ (-2\ln P_F)^{1/2}). \qquad \text{(V.15)}$$

can be obtained without computation. In Fig. 17 we have sketched P_D°, given

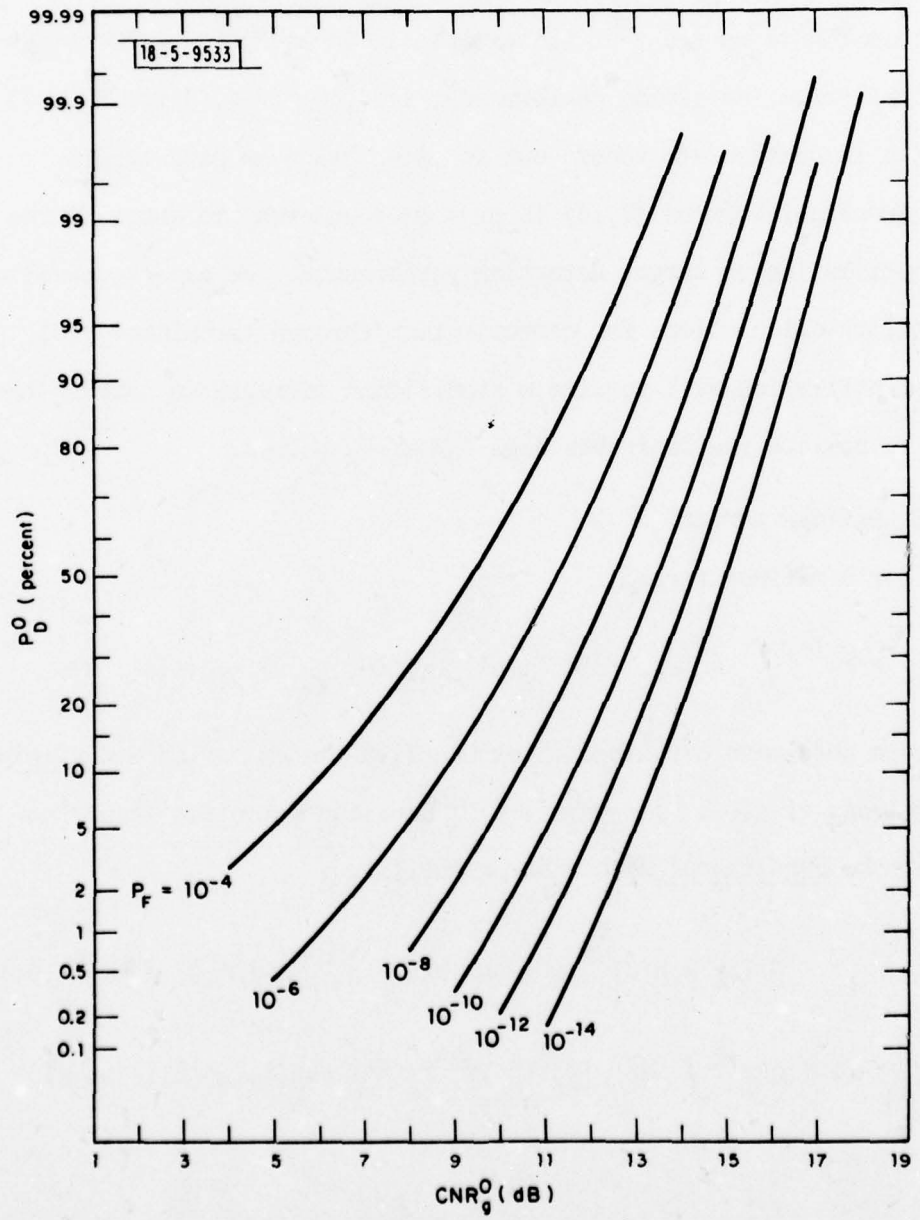

Fig. 17. Free-space propagation glint-target detection probability vs carrier-to-noise ratio for various false-alarm probability values.

by (V.15), vs. CNR°_{g} for a variety of interesting false alarm probabilities. From this figure we see that the example in Table 2, Fig. 11 will give excellent target detection performance, i.e., $P_D^{\circ} \geq 0.98$ for $P_F = 10^{-14}$ in a 2dB/km absorption atmosphere out to more than 6 km path length.

Numerical work on (V.14) is presently underway to quantify the effect of scintillation on target detection performance. We expect, based on error probability calculations for communication through turbulence [10], [39], that scintillation will require a significant increase in carrier-to-noise ratio to achieve the desirable high-P_D/low-P_F values.

Case 2 Diffuse target

For a diffuse target

$$\underline{Y} = P_T^{1/2} \int d\bar{\rho}' \, \underline{\xi}_t^2(\bar{\rho}') \, \underline{T}_s(\bar{\rho}') \exp(2\chi(\bar{\rho}', \bar{0}) + 2j\phi(\bar{\rho}', \bar{0}))$$

will be a zero-mean circulo-complex Gaussian random variable conditioned on knowledge of $\chi(\bar{\rho}', \bar{0}) + j\phi(\bar{\rho}', \bar{0})$. Gaussian detection theory now gives us [36] the conditional detection probability

$$\Pr[|\underline{Y} + \underline{n}(0)|^2 \geq (-2h\nu_o W/\eta) \ln P_F \; |\chi(\bar{\rho}',\bar{0}) + j\phi(\bar{\rho}',\bar{0})]$$

$$= P_F^{\left(1 + \eta P_T \lambda^2 \int d\bar{\rho}' \, |\underline{\xi}_t^2(\bar{\rho}')|^2 \, T_s(\bar{\rho}') \exp(4\chi(\bar{\rho}',\bar{0}))/2h\nu_o W\right)^{-1}}$$

(V.16)

Because sums of real-valued lognormal random variables are themselves approximately lognormal random variables [40], [41], the random variable u defined by

$$e^{2u} = \eta P_T \lambda^2 \int d\bar{\rho}' |\underline{\xi}_t^2(\bar{\rho}')|^2 T_s(\bar{\rho}') e^{4\chi(\bar{\rho}',\bar{0})} / 2h\nu_o WCNR_s \quad (V.17)$$

may be taken as Gaussian with mean $-\sigma^2$ and variance σ^2 where (assuming T_s is constant over the illumination region)

$$e^{4\sigma^2} = \frac{\int d\bar{\rho}_1' \int d\bar{\rho}_2' \; |\underline{\xi}_t^2(\bar{\rho}_1')|^2 \; |\underline{\xi}_t^2(\bar{\rho}_2')|^2 \exp(16C\chi\chi(\bar{\rho}_1' - \bar{\rho}_2', \bar{0}))}{\left(\int d\bar{\rho}' \; |\underline{\xi}_t^2(\bar{\rho}')|^2 \right)^2} \quad (V.18)$$

Equation (V.18) exhibits the aperture-averaging effect, viz, $e^{4\sigma^2} = 1 + \zeta(e^{16\sigma_\chi^2} - 1)$ where $\zeta \tilde{\approx} 1$ for $\lambda L/d < (\lambda L)^{1/2}$ and $\zeta \tilde{\approx} d^2/\lambda L$ for $\lambda L/d >> (\lambda L)^{1/2}$ (recall (IV.36)).

Using the above results we find that the detection probability is

$$P_D = \int_{-\infty}^{\infty} dU p_u(U) \; P_F^{\;(1 + CNR_s \exp(2U))^{-1}} \quad (V.19)$$

where $p_u(U) = (2\pi\sigma^2)^{-1/2} \exp[-(U + \sigma^2)^2/2\sigma^2]$. Equation (V.19) has not been evaluted in the literature; we have it under study at present. In the absence of turbulence we have $\sigma^2 = 0$ and (V.19) collapses to the well-known free space result

$$P_D^\circ = P_F^{\;(1 + CNR_s^\circ)^{-1}} \quad (V.20)$$

shown in Fig. 18. This figure shows that the example of Table 2, Fig. 12 will give good target detection performance, i.e., $P_D^\circ \geq 0.95$ for $P_F = 10^{-14}$ in a 2dB/km absorption atmosphere out to more than 4 km path length.

Comparison of Figs. 17 and 18 reveals that it is significantly easier to achieve high-P_D°/low-P_F values for a glint target than for a speckle target; for $P_D^\circ = 0.98$, $P_F = 10^{-14}$ the glint target requires a 17 dB carrier-to-noise ratio whereas the speckle target requires a 32 dB carrier-to-noise ratio. Paradoxically, it would seem, at low carrier-to-noise ratio it is easier to detect a speckle target than a glint target; for $P_F = 10^{-10}$ and 10 dB carrier-to-noise ratio we find $P_D^\circ = 0.014$ for a glint target and $P_D^\circ = 0.123$ for a speckle target. The explanation of the high-CNR disadvantage and the low-CNR advantage of the speckle target vs. the glint target is as follows. When $CNR_g^\circ = CNR_s^\circ$ the average strength of the randomly distributed speckle-target return equals the strength of the non-fluctuating glint-target return. At high carrier-to-noise ratios, speckle-target detection probability is limited primarily by the chance that a deep fade will occur (i.e., the target return is much weaker than its mean value and thus buried in the receiver noise), hence the disadvantage relative to a glint target. At low carrier-to-noise ratios, speckle-target detection probability is enhanced by the chance that the target return will be much stronger than its mean value and thus stand out from the receiver noise; this explains the performance advantage relative to a glint target.

VI. SUMMARY

In this section we shall summarize the key results of our imaging and

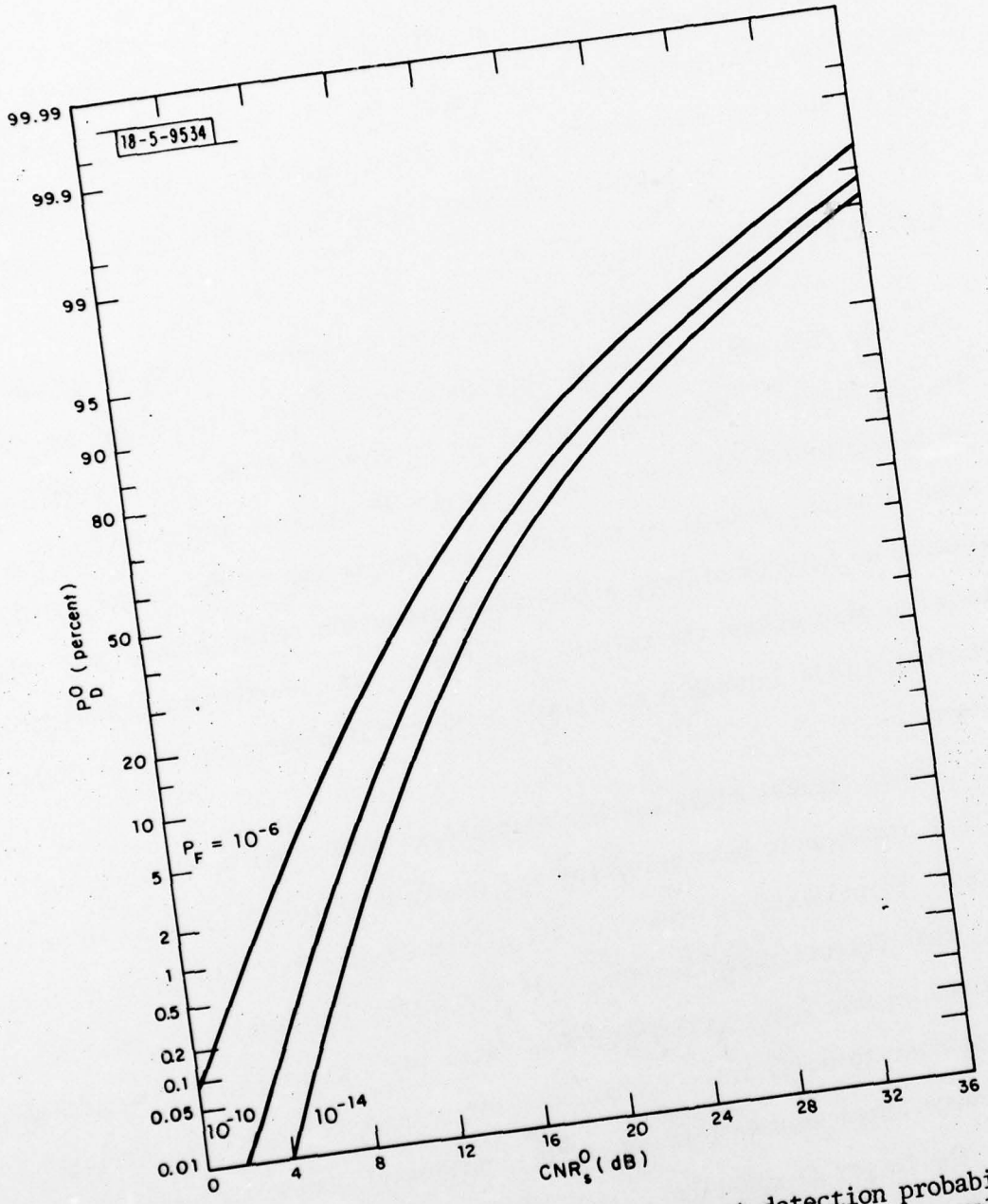

Fig. 18. Free-space propagation diffuse-target detection probability vs carrier-to-noise ratio for various false-alarm probability values.

target detection analyses. We shall draw freely from Sections II-V without explicitly stating the conditions required for the validity of the results, and we shall presume familiarity with the notation developed in those sections (see Table 3). We begin with a qualitative description of our theory.

Qualitative Radar Behavior

In all weather conditions for which atmospheric backscatter can be ignored, the radar receiver's IF signal consists of a target return plus receiver noise. The target return may be influenced by atmospheric beam spreading (which can reduce the on-target irradiance) and atmospheric scintillation, as well as the reflection properties of the target itself. Because we have considered a heterodyne reception radar, atmospheric coherence-loss can also affect the target-return IF signal. Furthermore, atmospheric absorption will introduce an overall exponential extinction of the target return.

Under typical clear-weather atmospheric conditions we shall have $d < \rho_o$, so that atmospheric beam spreading and receiver coherence-loss may be neglected. Scintillation, however, will play a significant role in both imaging and target-detection applications. In the former instance, scintillation will limit achievable image signal-to-noise ratio for a glint target observed under high carrier-to-noise ratio conditions; for a speckle target, scintillation may reduce image signal-to-noise ratio significantly below the unity level set by the target fluctuations. Multiframe averaging will be needed to overcome the scintillation limit on image signal-to-noise ratio.

TABLE 3

SUMMARY OF NOTATION

Radar Parameters

P_T = transmitter peak power

d = optics diameter

λ = 10.6μm wavelength

$h\nu_o$ = photon energy at 10.6μm wavelength

η = detector quantum efficiency

$2W$ = unilateral IF bandwidth

$\underline{\xi}_t$ = normalized target-plane illuminator beam

Atmospheric Parameters

χ = turbulence-induced log-amplitude fluctuation

ϕ = turbulence-induced phase fluctuation

ρ_o = field coherence length

L = path length

σ_χ^2 = log-amplitude variance

α = absorption coefficient

ζ = aperture-averaging factor

σ^2 = aperture-averaged log-amplitude variance

Target Parameters

$\underline{T}_s$ = diffuse-reflection coefficient

$\underline{T}_g e^{j\theta}$ = specular-reflection coefficient

A_T = target area

$\rho'(\lambda;\bar{f}_i;\bar{f}_r)$ = target bidirectional reflectance

T_s = average diffuse-reflection intensity coefficient

In single-pulse target detection, target speckle and/or scintillation dictate that receiver carrier-to-noise ratio must be increased (over that needed for a free-space propagation/glint-target system) to achieve the desirable combination of a high detection probability at a low false-alarm rate.

IF Signal Complex Envelope

Assuming $d < \rho_o$ and a target reflection coefficient with diffuse and single-glint components, we have that the IF signal complex envelope satisfies

$$\underline{r}(t) = \underline{y} + \underline{n}(t) \tag{VI.1}$$

where

$$\underline{y} \overset{\sim}{\sim} P_T^{1/2} \int d\bar{\rho}' \; \underline{\xi}_t^{\,2}(\bar{\rho}') \; \underline{T}_s(\bar{\rho}') \exp(2\chi(\bar{\rho}',\bar{0}) + 2j\phi(\bar{\rho}',\bar{0}) - \alpha L)$$

$$+ P_T^{1/2} \int d\bar{\rho}' \; \underline{\xi}_t^{\,2}(\bar{\rho}') \; \underline{T}_g(\bar{\rho}') \exp(2\chi(\bar{\rho}_g',\bar{0}) + 2j\phi(\bar{\rho}_g',\bar{0}) + j\theta - \alpha L), \tag{VI.2}$$

is the target return, and $\underline{n}(t)$, a zero-mean circulo-complex Gaussian noise process with spectral density

$$S_{nn}(f) = h\nu_o/\eta \quad \text{for } |f| \leq W, \tag{VI.3}$$

is the heterodyne-receiver shot noise.

Carrier-to-Noise Ratio

The carrier-to-noise ratio for the above IF signal envelope,

$$CNR = \langle|\underline{y}|^2\rangle \; / \; \langle|\underline{n}|^2\rangle, \tag{VI.4}$$

is given by

$$CNR = CNR_g + CNR_s \tag{VI.5}$$

in terms of its glint contribution (Fig. 11)

$$CNR_g = (\eta P_T/2h\nu_o W)\,|\underline{\xi}_t^{\,2}(\lambda L\bar{f}_T)|^2\;\lambda^2\;A_T\;\rho'(\lambda;\bar{f}_T;-\bar{f}_T)e^{4\sigma_\chi^2\;-2\alpha L}, \tag{VI.6}$$

and its speckle contribution (Fig. 12)

$$CNR_s = (\eta P_T/2h\nu_o W)\;\lambda^2\;T_s(\lambda L\bar{f}_T)\int d\bar{\rho}'\;\;|\underline{\xi}_t^{\,2}(\bar{\rho}')|^2\;e^{4\sigma_\chi^2\;-2\alpha L} \tag{VI.7}$$

Image Signal-to-Noise Ratio

The image signal-to-noise ratio,

$$SNR = \frac{(\langle|\underline{r}(0)|^2\rangle \; - \; 2h\nu_o W/\eta)^2}{Var(|\underline{r}(0)|^2)} \tag{VI.8}$$

satisfies

$$SNR = \frac{CNR/2}{1 \; + \; CNR/2SNR_{SAT} \; + \; (2CNR)^{-1}}\;, \tag{VI.9}$$

where

$$SNR_{SAT} \equiv \langle|\underline{y}|^2\rangle^2 \; / \; Var(|\underline{y}|^2) \tag{VI.10}$$

is the saturation signal-to-noise ratio (due to target and turbulence fluctuations). For CNR $\geq$ 5, (VI.9) reduces to the universal curve

$$\frac{SNR}{SNR_{SAT}} \approx \frac{CNR/2SNR_{SAT}}{1 + CNR/2SNR_{SAT}}, \qquad \text{(VI.11)}$$

which shows (Fig. 9) that increasing CNR beyond $2SNR_{SAT}$ does little to improve image signal-to-noise ratio.

The saturation signal-to-noise ratio, (VI.10), has the following behavior:

i) No turbulence, specular target

$$SNR^{\circ}_{gSAT} = \infty \qquad \text{(VI.12)}$$

ii) No turbulence, diffuse target

$$SNR^{\circ}_{sSAT} = 1 \qquad \text{(VI.13)}$$

iii) No turbulence, semi-rough target

$$SNR^{\circ}_{SAT} = 1 + CNR^{\circ}_{g}/CNR^{\circ}_{s} \qquad \text{(VI.14)}$$

iv) Turbulence, specular target (Fig. 13)

$$SNR_{gSAT} = (e^{16\sigma_{\chi}^2} - 1)^{-1} \qquad \text{(VI.15)}$$

v) Turbulence, diffuse target (Fig. 15)

$$SNR_{sSAT} = [1 + 2(e^{16\sigma_{\chi}^2} - 1)\zeta]^{-1} \qquad \text{(VI.16)}$$

Likelihood-Ratio Test

The decision rule which maximizes the conditional probability you say a target is present given there is one present, subject to the constraint

that the conditional probability you say a target is present given there is no target there, is the threshold test

$$\begin{array}{c} \text{say } H_1 \\ \geq \\ |\underline{r}(0)|^2 \qquad -(2h\nu_o W/\eta)\ell n\, P_F \\ < \\ \text{say } H_0 \end{array} \tag{VI.17}$$

Receiver Operating Characteristic

The threshold test (VI.17) has false alarm probability P_F and detection probability given as follows:

i) No turbulence, specular target (Fig. 17)

$$P_D^\circ = Q_M((2CNR^\circ_g)^{1/2},\ (-2\ell n\, P_F)^{1/2}) \tag{VI.18}$$

where Q_M is Marcum's Q function

ii) No turbulence, diffuse target (Fig. 18)

$$P_D^\circ = P_F^{(1 + CNR^\circ_s)^{-1}} \tag{VI.19}$$

iii) Turbulence, specular target

$$P_D = \int_{-\infty}^{\infty} d\chi\ P_\chi(\chi)\ Q_M((2CNR^\circ_g)^{1/2}\ e^{2\chi}, (-2\ell n\, P_F)^{1/2}) \tag{VI.20}$$

where $P_\chi(\chi) = (2\pi\sigma_\chi^2)^{-1/2}\ \exp[-(\chi + \sigma_\chi^2)^2/2\sigma_\chi^2]$

iv) Turbulence, diffuse target

$$P_D = \int_{-\infty}^{\infty} dU p_u(U)\ P_F^{\ (1 + CNR_s \exp(2U))^{-1}} \qquad \text{(VI.21)}$$

where $p_u(U) = (2\pi\sigma^2)^{-1/2} \exp[-(U + \sigma^2)^2/2\sigma^2]$

ACKNOWLEDGMENTS

This report would not have been possible without the encouragement of A. B. Gschwendtner and H. Kleiman, and useful technical discussions with R. C. Harney and R. J. Becherer. Their support and guidance is gratefully acknowledged.

REFERENCES

1. R. J. Becherer, "Pulsed Laser Ranging Techniques at 1.06 and 10.6 μm," Project Report TT-8, Lincoln Laboratory, M.I.T. (19 March 1976), DDC AD-A024557/1.

2. R. J. Becherer, "System Design Study for Infrared Airborne Radar (IRAR)," Technical Note 1977-29, Lincoln Laboratory, M.I.T. (18 October 1977), DDC AD-A048979/9.

3. R. M. Lerner and A. E. Holland, "The Optical Scatter Channel," Proc. IEEE 58, 1547-1563 (1970).

4. E. A. Bucher, "Computer Simulation of Light Pulse Propagation for Communication through Thick Clouds," Appl. Opt. 12, 2391-2400 (1973).

5. E. A. Bucher and R. M. Lerner, "Experiments on Light Pulse Communication and Propagation through Atmospheric Clouds," Appl. Opt. 12, 2401-2414 (1973).

6. W. H. Paik, M. Tebyani, D. J. Epstein, R. S. Kennedy and J. H. Shapiro, "Propagation Experiments in Low-Visibility Atmospheres," Appl. Opt. 17, 899-905 (1978).

7. R. S. Lawrence and J. W. Strohbehn, "A Survey of Clear-Air Propagation Effects Relevant to Optical Communications," Proc. IEEE 58, 1523-1545 (1970).

8. E. Brookner, "Atmospheric Propagation and Communication Channel Model for Laser Wavelengths," IEEE Trans. Commun. Technol. COM-18, 396-416 (1970).

9. R. L. Range, "Electromagnetic Beam Propagation in Turbulent Media," Proc. IEEE 63, 1669-1692 (1975).

10. J. H. Shapiro, "Imaging and Optical Communication through Atmospheric Turbulence," (to appear in J. W. Strohbehn (Ed.), Laser Beam Propagation through the Atmosphere, Springer-Verlag, Berlin).

11. J. W. Goodman, "Some Effects of Target-Induced Scintillation on Optical Radar Performance," Proc. IEEE 53, 1688-1700 (1965).

12. J. C. Dainty, ed., Laser Speckle and Related Phenomena (Springer-Verlag, Berlin 1975).

13. D. L. Fried, "Statistics of the Laser Radar Cross Section of a Randomly Rough Target," J. Opt. Soc. Am. 66, 1150-1160 (1976).

14. R. M. Gagliardi and S. Karp, Optical Communications (Wiley, New York 1976) Chapter 6.

15. J. H. Shapiro, "Reciprocity of the Turbulent Atmosphere," J. Opt. Soc. Am. 61, 492-495 (1971).

16. J. H. Shapiro, "Optimal Power Transfer through Atmospheric Turbulence Using State Knowledge," IEEE Trans. Commun. Technol. COM-19, 410-414 (1971).

17. J. H. Shapiro, "Point-Ahead Limitation on Reciprocity Tracking," J. Opt. Soc. Am. 65, 65-68 (1975).

18. J. H. Shapiro, "Propagation-Medium Limitations on Phase-Compensated Atmospheric Imaging," J. Opt. Soc. Am. 66, 460-469 (1976).

19. A. E. Siegman, "The Antenna Properties of Optical Heterodyne Receivers," Proc. IEEE 54, 1350-1356 (1966).

20. Target Signature Analysis Center: Data Compilation, Eleventh Supplement, Volume 1 - Bidirectional Reflectance: Definition, Discussion, and Utilization and Volume 2 - Bidirectional Reflectance: Graphic Data, AFAL-TR-72-226 (1972).

21. J. W. Strohbehn, ed. Laser Beam Propagation through the Atmosphere, (Springer-Verlag, Berlin, in press).

22. H. S. Lin, "Communication Model for the Turbulent Atmosphere," Ph.D. Thesis, Department of Elect. Engr. and Appl. Phys., Case Western Reserve Univ., August 1973.

23. R. F. Lutomirski and H. T. Yura, "Propagation of a Finite Optical Beam in an Inhomogeneous Medium," Appl. Opt. 10, 1651-1663 (1971).

24. H. T. Yura, "Mutual Coherence Function of a Finite Cross-Section Optical Beam Propagating in a Turbulent Medium," Appl. Opt. 11, 1399-1406 (1972).

25. A. Kon and V. Feizulin, "Fluctuations in the Parameters of Spherical Waves Propagating in a Turbulent Atmosphere," Radiophys. Quantum Electron. 13, 51-53 (1970).

26. J. W. Goodman, Introduction to Fourier Optics, (McGraw-Hill, New York, 1968) chapters 3, 4.

27. P. Beckmann and A. Spizzichino, The Scattering of Electromagnetic Waves from Rough Surfaces, (Pergamon, Oxford, 1963).

28. Special issue on Speckle in Optics J. Opt. Soc. Am. 66, 1145-1313 (1976).

29. R. L. Mitchell, "Models of Extended Targets and Their Coherent Radar Images," Proc. IEEE 62, 754-758 (1974).

30. M. Skolnik, ed. Radar Handbook, (McGraw-Hill, New York, 1970).

31. E. Brookner, ed. Radar Technology (Artech, Dedham, 1977).

32. H. L. Van Trees, Detection, Estimation and Modulation Theory, Part III, (Wiley, New York, 1971) chapter 13.

33. M. Born and E. Wolf, Principles of Optics, 5th edition, (Pergamon, Oxford, 1975) appendix III.

34. D. L. Fried, "Aperture Averaging of Scintillation," J. Opt. Soc. Am. 57, 169-175 (1967).

35. H. L. Van Trees, Detection, Estimation, and Modulation Theory, Part I, (Wiley, New York, 1968) Chapter 2.

36. H. L. Van Trees, Detection, Estimation, and Modulation Theory, Part I, (Wiley, New York, 1968) chapter 4.

37. J. Marcum, "A Statistical Theory of Target Detection by Pulsed Radar," IEEE Trans, Inform. Theory IT-6, 59-267 (1960).

38. J. Marcum, "Table of Q-Functions," Rand Corporation Rpt. RM-339, January 1, 1950.

39. E. V. Hoversten, R. O. Harger, and S. J. Halme, "Communication Theory for the Turbulent Atmosphere," Proc. IEEE 58, 1626-1650 (1970).

40. R. L. Mitchell, "Permanence of the Lognormal Distribution," J. Opt. Soc. Am. 58, 1267-1272 (1968).

41. B. K. Levitt, "Detector Statistics for Optical Communication through the Turbulent Atmosphere," Quart. Progr. Rpt. 99, Research Lab. Electron., M.I.T.,114-123, October 1970.

UNCLASSIFIED

SECURITY CLASSIFICATION OF THIS PAGE *(When Data Entered)*

REPORT DOCUMENTATION PAGE

READ INSTRUCTIONS BEFORE COMPLETING FORM

1. REPORT NUMBER: ESD-TR-78-275
2. GOVT ACCESSION NO.
3. RECIPIENT'S CATALOG NUMBER

4. TITLE (and Subtitle): Imaging and Target Detection with a Heterodyne-Reception Optical Radar
5. TYPE OF REPORT & PERIOD COVERED: Project Report
6. PERFORMING ORG. REPORT NUMBER: Project Report TST-24

7. AUTHOR(s): Jeffrey H. Shapiro
8. CONTRACT OR GRANT NUMBER(s): F19628-78-C-0002

9. PERFORMING ORGANIZATION NAME AND ADDRESS
Lincoln Laboratory, M.I.T.
P.O. Box 73
Lexington, MA 02173

10. PROGRAM ELEMENT, PROJECT, TASK AREA & WORK UNIT NUMBERS
Program Element No. 65705F
Project No. 649L

11. CONTROLLING OFFICE NAME AND ADDRESS
Air Force Systems Command, USAF
Andrews AFB
Washington, DC 20331

12. REPORT DATE: 13 October 1978
13. NUMBER OF PAGES: 84

14. MONITORING AGENCY NAME & ADDRESS *(if different from Controlling Office)*
Electronic Systems Division
Hanscom AFB
Bedford, MA 01731

15. SECURITY CLASS. *(of this report)*: Unclassified

15a. DECLASSIFICATION DOWNGRADING SCHEDULE

16. DISTRIBUTION STATEMENT *(of this Report)*

Approved for public release; distribution unlimited.

17. DISTRIBUTION STATEMENT *(of the abstract entered in Block 20, if different from Report)*

18. SUPPLEMENTARY NOTES

None

19. KEY WORDS *(Continue on reverse side if necessary and identify by block number)*

infrared airborne radar
heterodyne reception
imaging
target detection
signal-to-noise ratio
matched filters
target speckle
glint
atmospheric scintillation
atmospheric turbulence

20. ABSTRACT *(Continue on reverse side if necessary and identify by block number)*

A theoretical study of the use of a heterodyne reception CO_2 laser radar for imaging and target detection is reported. Specifically, a mathematical system model for the radar is developed, incorporating the statistical effects of propagation through atmospheric turbulence, target speckle and glint, and heterodyne-reception shot noise. This model is used to find the image signal-to-noise ratio of a matched-filter envelope detector receiver and the target-detection probability of the optimum likelihood-ratio processor. For realistic parameter values it is shown that turbulence-induced beam spreading and coherence loss may be neglected. Target speckle and atmospheric scintillation, however, present serious limitations on single-frame imaging and target detection performance.

DD FORM 1 JAN 73 1473 EDITION OF 1 NOV 65 IS OBSOLETE

UNCLASSIFIED

SECURITY CLASSIFICATION OF THIS PAGE *(When Data Entered)*

207650